Study on magnetism in kagome-lattice compound $MgMn_3(OH)_6Cl_2$

September 2020

Department of Science and Advanced Technology

Graduate School of Science and Engineering

Saga University

Md. Mahbubur Rahman Bhuiyan

Abstract

Geometrical frustration usually causes due to the lattice's geometry has become a subject of recent intensive experimental and theoretical work. The spin frustration found in triangular, pyrochlore, and kagome lattice geometry has a large degenerate ground state that suppresses long-range order (LRO) and capable of new quantum stated like spin liquid, spin nematic, and spin ice, etc. A large number of experimental and theoretical studies on the kagome antiferromagnet have been accomplished to explore the magnetism in it. The experimental investigation revealed that changing the spin moment from lower to higher value, spin liquid diminish which allows the compound to be long-range magnetic ordered. It has been reported that the long-range order is intrinsic in the classical Heisenberg spin system. Therefore, the evolution of magnetism in the higher spin moment (S = 5/2) classical system $MgMn_3(OH)_6Cl_2$, which is the end classical spin compound in the transition metal hydroxyhalogenide series has become interesting in the scientific and technical point of views.

The synthesis, structural, and magnetic characterization of an S = 5/2 classical spin kagome compound $MgMn_3(OH)_6Cl_2$ will be the subject of interest to know the ground state of this spin system. The white coloured polycrystalline $Mg_xMn_{4-x}(OH)_6Cl_2$ compound has been successfully synthesized by selectively substituting the triangular-lattice plane Mn^{2+} with non-magnetic Mg^{2+}. The compound crystallizes in rhombohedral structure in space group R-3m, in a similar crystal structure to the much-researched quantum spin liquid candidates herbertsmithite $ZnCu_3(OH)_6Cl_2$ and tondiite $MgCu_3(OH)_6Cl_2$. The temperature dependant magnetic susceptibility reveals antiferromagnetic transition below T_N ~ 8 K. The neutron powder diffraction experiment confirmed long-ranged magnetic order developed below T_N ~ 8 K. The obtained value of critical exponent β = 0.35, agrees with a 3D Heisenberg spin system with 120° nearest-neighbor spin structure confined in the kagome plane with spin-vector chirality of q = +1 below the transition temperature (T_N). Since the transition temperature in the $Mg_xMn_{4-x}(OH)_6Cl_2$ compound lies between 7.6 - 8 K, present work suggests the intrinsic nature of long-range order in classical Heisenberg kagome antiferromagnet and provides a classical reference system to quantum kagome antiferromagnets.

Contents

List of Figures

Chapter-1: Magnetism, Geometrical Frustration

List of Tables

Chapter-1

Magnetism, Geometrical Frustration

1.1. Introduction

The phenomenon of magnetism in solids has received a lot of interest since ancient times because of scientific and technological importance. The advancement in the field of magnetism has started from the studies of strongly correlated electron system in which the collective interaction between the electrons is treated by quantum mechanical effect and provides the opportunity to find novel states of matter. The geometrical frustration which is supposed to arise due to lattice geometry of the crystal for which the coupling between the lattice and the spin makes it difficult for a system to gain the lowest possible energy states has been playing a central role to induce such novel states of matter. The competition between the lattice frustration and the exchange interaction in the frustrated system results in unconventional ground states like spin liquid, spin ice, and spin nematic, etc**.** [1-3]. Geometrical frustration is usually found in 3D-pyrochlore lattice, triangular lattice, and kagome lattice geometry. The kagome lattice is suitable to understand the noble states like spin liquid in solids because of having large degenerate ground states in comparison to other lattice geometry. The constituents spin in the spin liquid are highly correlated but fluctuating strongly down to low temperature. The spin liquid can be classical and quantum, depending on the spin moment. The experimental observation of $S = 1/2$ quantum spin kagome herbertsmithite [4-5] complies with the theoretical prediction for quantum spin liquid, whereas there is a discrepancy between the experimental results of $S = 2$ quasi-classical spin kagome $MgFe_3(OH)_6Cl_2$ [6] and theoretical prediction of classical kagome lattice, which lead us to explore the ground state of classical spin kagome to search the interlaying physics inside it.

1.2. Geometrical Frustration

Geometrical frustration in a magnetic solid arises due to the geometry of the magnetic lattice and having different types of conflicting interaction [1], which results in a large number of ground state at zero temperature along with unusual thermal ordering. The simplest example of geometrical frustration in two-dimensional triangular lattices in which Ising spin resides in the vertices of the triangles as sketched in Fig.1.1 (a). The energy is minimized when each spin is aligned opposite to neighbors. Once the first two spins align anti-parallel, the third one is in frustration because it has two possible orientations of the spins, either up or down. The third spin cannot simultaneously minimize its interactions with the other two spins. Since this effect could occur for each spin, the ground state of this lattice geometry exhibits six-fold degeneracy, as depicted in Fig 1.1(a).

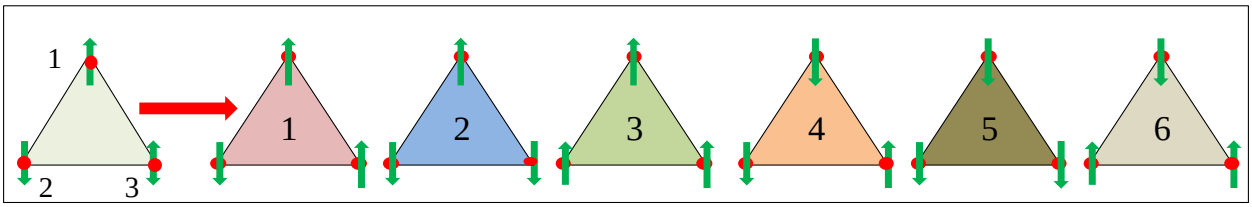

(a)

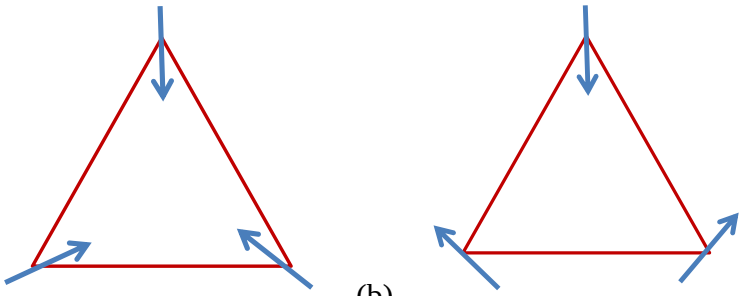

(b)

Figure 1.1. (a) Ising spins at the vortices of triangular plaquettes along with six-fold degeneracy, (b) examples of compromise Heisenberg or XY 120º spin structure that form on triangular plaquettes.

The spin system can also be frustrated with various types of conflicting interactions [1]. If we consider a chain of spins, whether the nearest neighbor (*nn*) interaction J_1 is ferromagnetic and the next nearest neighbor (*nnn*) interaction J_2 is antiferromagnetic nature. When $|J_2|<<J_1$, the ground state is ferromagnetic; every nearest neighbor (*nn*) is satisfied, but the next nearest neighbor (*nnn*) interaction does not satisfied. When $|J_2|$ exceeds a critical value, the ferromagnetic ground state will no longer valid; both the *nn* and *nnn* bonds are not completely satisfied. Therefore, the spin system is frustrated when the two interacting spins do not satisfy each other completely. Apart from the Ising spin, XY and Heisenberg spin on the vertices of a triangular lattice form a ground state that is a compromise canted configuration of spins with the neighbors at 120^o to one another [7], as depicted in Fig 1.1(b). Macroscopic ground state degeneracy forms in edge-sharing or vortex-sharing triangles. Moreover, the degeneracy depends on the nature of connectivity, whether it is edge-sharing or vertex-sharing. The low lattice connectivity reduces the constraint on individual spins and increases the number of degree-of-freedom in the ground state.

Geometrical frustration is usually found in the lattice, which is composed of side-sharing triangles and of corner-sharing triangles. Pyrochlore, triangular, and kagome lattice geometry composed such triangles offer frustration. Geometrical frustration suppresses long-range order by reducing the transition temperature with respect to Curie-Weiss temperature (θ_{CW}). Frustration is quantified by the ratio of Curie –Weiss temperature to transition temperature by $f = |\theta_{cw}|/T_N$. Ramirez A. P [8] has set up some criteria for geometrical frustration, which are presented in Table 1.1.

Table 1.1. Criterions for a lattice system to be geometrically frustrated as set by Ramirez A.P.

No.	Frustration Index	Type of frustration
1.	$f = 1$	Un-frustrated
2.	$1 < f < 10$	Moderate frustration
3.	$f > 10$	Strong frustration

1.3. Geometrically Frustrated Lattices

The connectivity of triangular units and lattice dimensionality are structural features to destabilize conventional magnetic order alongside the geometrical frustration of the triangular plaquettes. The ground state degeneracy is large (system with low connectivity, e.g., vertex-sharing triangles) and magnetic order being destabilized for low-dimensionality systems. Based on the low connectivity and dimensionality, the frustrated system can be sub-divided into three groups, namely- pyrochlore lattice made up of vertex-sharing tetrahedra and the 2-dimensional triangular and kagome lattices which are made up of edge-sharing and vertex sharing triangles, respectively. Brief descriptions of all of them are given here.

1.3.1. Pyrochlore-3D Frustrated Lattice

The most studied family of 3-dimensional frustrated lattices exhibit general formula $A_2B_2O_7$; A and B are rare-earth or transitional metal ion treated as a playground of geometrical frustration. The rare-earth pyrochlore structure is cubic in which A and B cation arranged in separate interpenetrating lattices of vortex-sharing tetrahedra as displayed in Fig. 1.2 (a). The A site is occupied by a rare earth element whose physical and chemical properties depend on its 4*f* electronic shell occupation [9-10]**.** The strong frustrated nearest neighbor (*nn*) interaction, next-nearest neighbor (*nnn*) exchange interaction, Dzyaloshinskii–Moriya (DM) exchange, dipolar interaction, and magneto-elastic couplings all are associated to the development of spin-spin correlation, which results in the formation of novel magnetic effects like spin-liquid, spin-glass, or disordered spin-ice states, etc. [11-12].

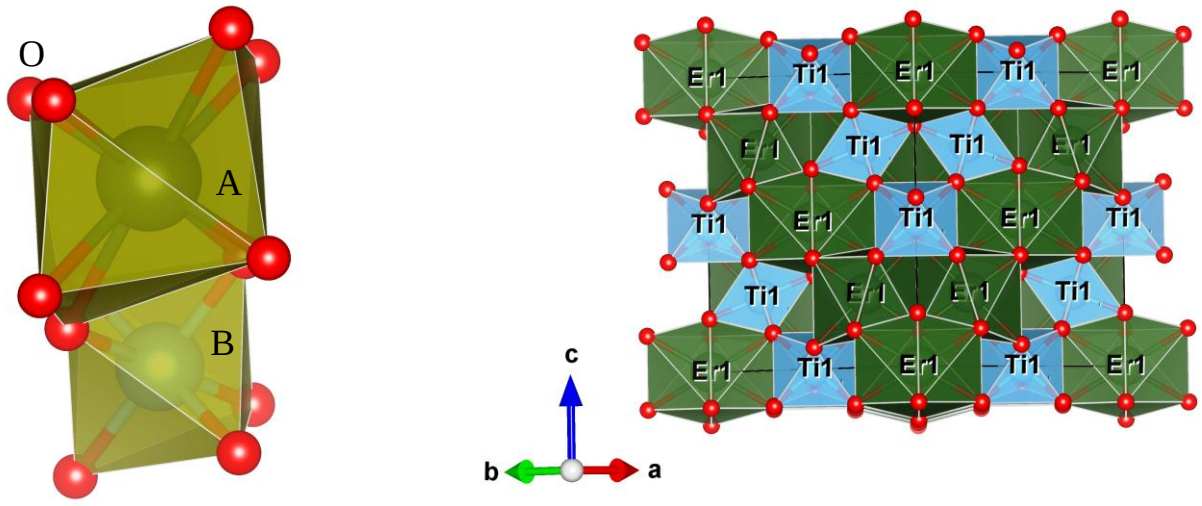

(a) (b)

Figure 1.2. (a) Typical pyrochlore structure in which A (rare earth atom) and B (transition magnetic atom) site alternatively stack on each other forming complete pyrochlore lattice structure, (b) crystal structure of one of the representative pyrochlore compound $Er_2Ti_2O_7$ in which erbium (Er) and titanium (Ti) atoms alternatively stack forming one other. Geometrical frustration is supposed to arise due to the unequal triangular arms of the octahedra of this compound. (Reproduced from [13]).

The most studied pyrochlore $Er_2Ti_2O_7$ compound, whose crystal structure is similar to Fig. 1.1(b) is considered to have a frustrated magnet and XY antiferromagnet [14]. The other rare-earth titanate family $R_2Ti_2O_7$ displays a wide range of exotic magnetic ground states like spin liquid state [15-17]. The materials with pyrochlore structure have been found to be used as ionic conductors, electronic insulators, superconducting materials (e.g., $Cd_2Re_2O_7$) [18], etc.

1.3.2. Triangular Lattice Geometry

Triangular lattice is the simplest geometrically frustrated system in two dimensions space that consists of edge-sharing triangles, which is depicted in Fig. 1.3 (a). Two spins can easily

accommodate two sides of the triangle while the third spin is frustrated. If this third spin is up, then two arrangements out of the three are compatible; but one is incompatible. This leads to a large degeneracy in the ground state along with non-zero entropy. Despite its lower degeneracy compared to the vertex-sharing geometries, the triangular lattice is predicted to host exotic physics, including unconventional phase transitions [19-21] and skyrmion spin structures. Quantum spin liquid state has been observed in triangular lattices *k* - $(BEDT\text{-}TTF)_2Cu_2(CN)_3$, $CsCeSe_2$, and $CsYbSe_2$ [22-23] because of having exotic ground states. Moreover, long-range order has been suppressed in the high spin triangular lattice $CsCoCl_3$ [24].

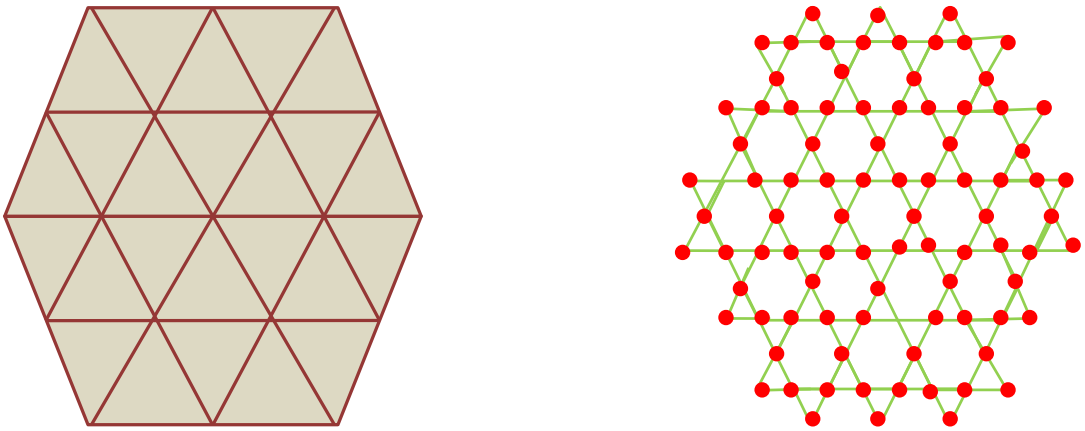

(a) (b)

Figure 1.3. Schematic view of (a) triangular lattice composed of edge-sharing triangles and (b) kagome lattice build with vortex-sharing triangles.

1.3.3. Kagome Lattice Geometry

The kagome lattice consists of vortex-sharing triangles rather than an edge-sharing triangle in two-dimensional triangular lattices, as depicted in Fig. 1.1 (b), which has been treated as the model systems to explore frustrated magnetism as the lattices' low-connectivity produces a macroscopically degenerate ground state predicted to prevent magnetic order at $T = 0$ [25]. They are also thought to exhibit many essential features of high-temperature superconductors [26].

Geometrical frustration can easily be understood in vortex sharing kagome lattice with respect to the edge-sharing triangular lattice. The spin arrangement of two adjacent triangles in triangular and kagome lattice is presented in Fig. 1.4 (a-c). All the upper triangles in Fig. 1.4 (a-c) exhibit spin chirality +1 (when the spin rotates clockwise with 120º spin steps). The neighboring triangle in the edge-sharing triangular lattice has to have chirality -1 (spin rotate anti-clockwise with 120º spin steps) to minimize total exchange energy. As a result, the spin configuration at the bottom triangle is unlikely determined.

On the other hand, the neighboring triangles [i.e., bottom triangle in Fig. 1.4 (b-c)] in the kagome lattice have two choices: chirality +1 or chirality -1 with identical minimized energies. Since two neighboring triangles in the kagome lattice share one common spin, the

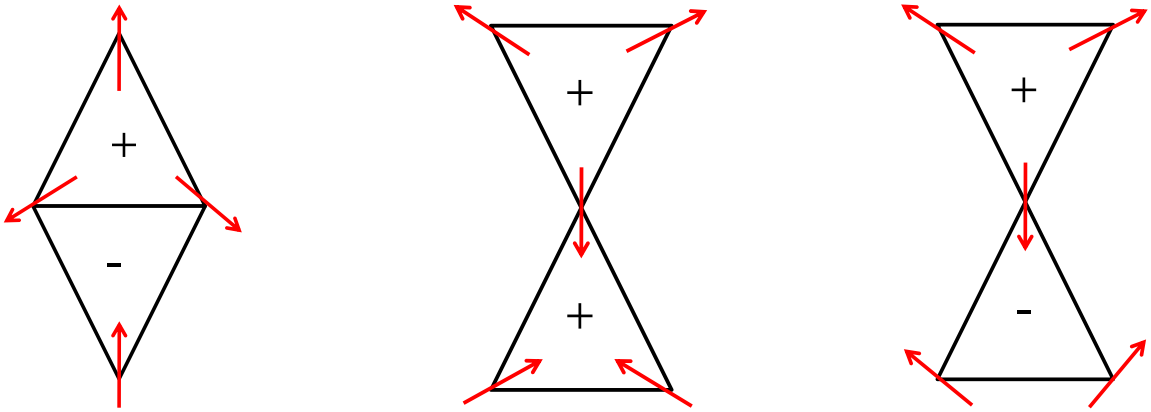

Figure 1.4. Spin arrangement in two neighboring, (a) edge-sharing triangles, (b-c) vortex-sharing triangles with chirality +1, and chirality -1.

upper triangle spin configuration has less influence on the bottom triangle spin in compared to edge-sharing triangular lattice in which two neighboring triangles share two common spins. This discrepancy gave higher degeneracy (or strong frustration) in the kagome lattice compounds. The crystal structure of jarosite and herbertsmithite mineral has kagome lattice geometry, which has already displayed novel physical properties.

1.4. Exotic Ground States

Magnetism in solids is the result of magnetic moments related to individual electrons [27-28]. The magnetic materials are usually classified as diamagnetic, paramagnetic, ferromagnetic, antiferromagnetic, and ferrimagnetic. The last three have been treated as ordered magnetism related to the exchange interaction. The disorder in solids is the consequence of geometrical frustration can lead to the formation of unconventional ground states that do not break the symmetry and have complex types of ordering, like, spin ice, spin-liquid (QSL), and spin nematic, which would be discussed here to introduce exotic ground state.

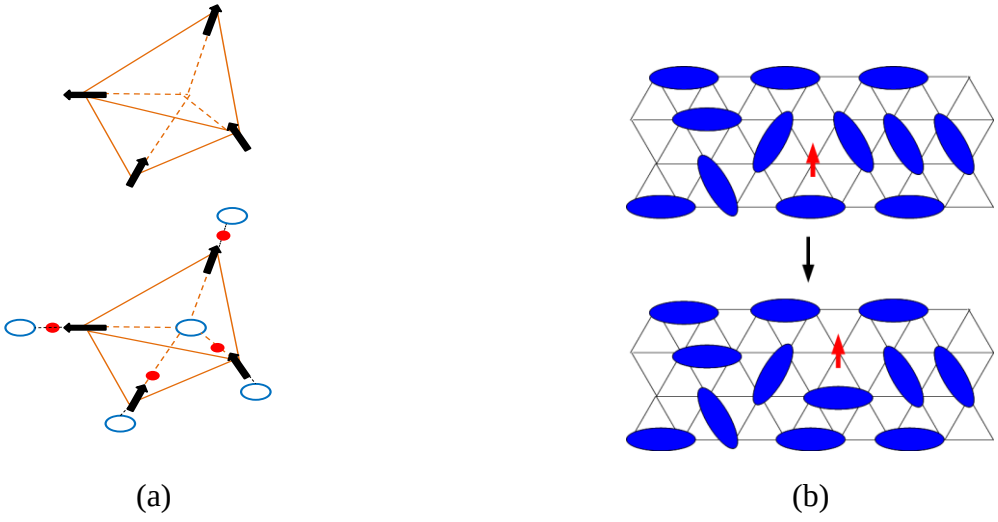

(a) (b)

Figure 1.5. (a) spin ice and water ice, and (b) spinon moving in spin liquids.

1.4.1. Spin Ice

Spin ice is a substance that is similar to water ice in that it can never be completely frozen because of a lack of a single minimal-energy state. The spin degree of freedom of spin ice with frustrated interaction prevents it from freezing. The low-temperature properties are displayed by spin ice, particularly residual entropy, closely related to crystalline water ice. The magnetic

ordering of spin ice resembles the positional ordering of hydrogen atoms in conventional water ice, as shown in Fig. 5 (a).

1.4.2. Spin Liquid (SL)

The spin liquid is the state of matter that does not display any ordering down to zero temperature without breaking symmetry, characterized by their long-range quantum entanglement, fractionalized excitation, and absence of ordinary magnetic order. Moreover, strong antiferromagnetic interaction with spinion moving through the materials is found in the spin liquid state [29]. The movement of spinion in the spin liquid state is as presented Fig. 5(b). Spin liquid could be classical or quantum, depending on the spin moment [30]. Several experimental techniques have been used to identify the spin liquid state in materials. Since many theoretical works have been accomplished on spin liquids, practical spin liquid materials have not yet been found. Some of the materials having spin liquid ground states are *k*-(BEDT-TTF)$_2$Cu$_2$(CN)$_3$ and $Ba_3CuSb_2O_9$ [31-32].

1.4.3. Spin Nematic

The molecules in the liquid crystal break the rotational symmetries of the space without breaking its translational symmetries. Similarly, the magnetic moments in the nematic spin phase break the spin-rotational symmetries without breaking the time-reversal symmetry [33-35]. The quadrupolar ordering may easily form a spin-nematic state in the materials. When complex order parameters break the spin-rotation symmetry, such spin-nematic phases are predicted to form from the interplay of various interactions, including geometric frustration [36], biquadratic exchange [37], competing anti-and ferromagnetic exchange [38], and bond based order parameters [39]. The nematic spin phase is found in the layered triangular-lattice magnet $NiGa_2S_4$ [40].

1.5. Phase transition and Magnetic Models

The phase transition utilizes the Landau theory [41] of the second-order phase transition to describe the states of the system in which the concept of the order parameter is an important factor. The non-zero value of the order parameter corresponds ordered phase at a temperature below the transition temperature (T_C), whereas the zero value of the order parameter offers a disordered phase above the transition temperature (T_C). The order parameter is the spontaneous magnetization for ferromagnet-

$$m = \frac{1}{N}\sum_i S_i \qquad (1.1)$$

In which, S_i represents the spin at *i*th state, and *N* is the total number of sites present in the lattice.

The staggered magnetization represents the ordered parameter for antiferromagnets-

$$m^* = \frac{1}{N}\sum_i S_i e^{i\vec{k}.\vec{r}} \qquad (1.2)$$

Where $\vec{r}$ and $\vec{k}$ are the position of spin and wave vector, respectively.

The magnetic phase transition is described according to Landau's theory based on the assumption that the free energy of a system can be expanded in terms of the order parameter. The free energy of a simple and homogeneous system with a spatially uniform order parameter (*m*) can be written as-

$$F = F_0 + V(\frac{1}{2}rm^2 + \frac{1}{4}um^4 + \frac{1}{6}vm^6 - \frac{mH}{k_BT} + \qquad (1.3)$$

The coefficients *r*, *u*, and *v* are dimensionless, and *V* is the system's volume.

In the second-order phase transition, the order parameter's increment is continuous, starting from zero at the critical temperature. In the magnetic system, the first derivative of free energy with respect to order parameter (m) is continuous, i.e., $\frac{\delta F}{\delta m} = 0$. Three solutions would be available after solving Eq. (1.3) using the condition $\frac{\delta F}{\delta m} = 0$, which yields-

$$m = 0 \qquad (1.4)$$

$$m = \pm\sqrt{-r/u} = \pm(\frac{r^{'}T_C}{u})^{\frac{1}{2}}(1 - \frac{T}{T_C})^{\frac{1}{2}} \qquad (1.5)$$

Here, $r = r^{'}(T - T_C)$ by expanding r in the vicinity of T_C. The solution at Eq. (1.4) represents the disordered state at $T > T_C$; whereas the solution at Eq. (1.5) corresponds to the behavior below T_C. The free energy F (m) as a function of magnetization (m) and temperature (T) is plotted in Fig. 1.6 (a), whereas the change of magnetization (m) with respect to temperature depicted in Fig 1.6 (b).

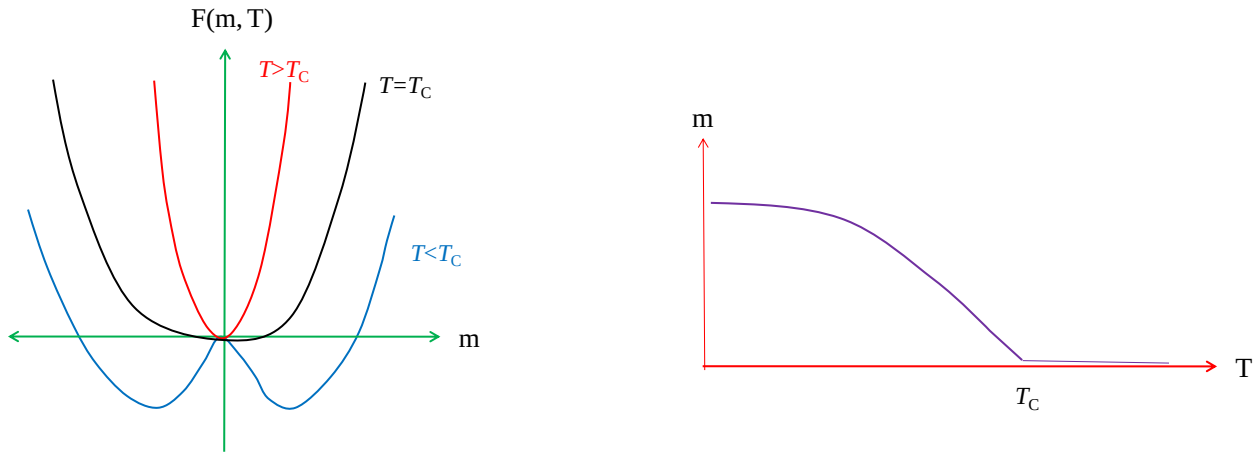

(a) (b)

Figure 1.6. (a) Free energy as a function of magnetization (m) and temperature (T), (b) magnetization is non-zero below the critical temperature. Reproduce from [42].

The Fig 1.6 (a) clearly displayed F(m) have only one global minimum at $T > T_C$; there are two degenerate non-trivial global minima at $T < T_C$; whereas at $T = T_C$ gives a large number of degenerate ground states that are fluctuating around the global minima $m = 0$.

The thermodynamic properties of a system could be represented by a set of power-law near the critical temperature (T_C). The order parameter for magnetic systems (m), specific heat (C), susceptibilities (χ), and correlation length (ξ) are summarized as-

$$m = m_0|1 - \frac{T}{T_C}|^{\beta} \quad (1.6)$$

$$\chi = \chi_0|1 - \frac{T}{T_C}|^{-\gamma} \quad (1.7)$$

$$C = C_0|1 - \frac{T}{T_C}|^{-\alpha} \quad (1.8)$$

$$\xi = \xi_0|1 - \frac{T}{T_C}|^{-\nu} \quad (1.9)$$

Here β, γ, α, and ν are treated as the critical exponent, which depends on the type of system giving valuable information about the nature of phase transition. The critical exponents have the values according to Landau theory-

$$\beta = \frac{1}{2}, \qquad \gamma = 1, \qquad \alpha = 0, \quad and\ \nu = \frac{1}{2} \quad (1.10)$$

Based on the obtained values of critical exponent, the second-order continuous phase transitions are mainly dependent on the dimensionality of the order parameter (D), e.g., spin; dimensionality of the system (d), and type of forces, whether short or long-range. The mean-field model is suitable to describe the phase transitions when systems have high lattice dimensionality and long-range interactions. Magnetic order is less favorable for the systems with low lattice-dimensionality because of increased entropy of magnetic defects [43]. For example, a 1-dimensional lattice of spins can never order because a defect's energy cost remains constant, but

the entropy continues to increase. So as long as T > 0, the free energy is negative and a defect can occur spontaneously from anywhere in the system to prevent long-range magnetic order. Whether the dimensionality of lattice increased, the cost of energy for defects raises so that for d > 3, magnetic order is always possible. Unconventional phase transitions are possible in the case of intermediated = 2 system. There are three magnetic models for three different values of D, which are-

Ising model: The coupling of spin points along the local *z*-direction. The spin at each lattice site could have spin state '*S*' in one of the two states (+1, or -1). These spins are allowed to interact with their neighbors. Neighboring spins that agree have lower energy than those that disagree; the system tends to the lowest energy, but heat disturbs this tendency, thus creating the possibility of different structural phases. The two-dimensional square lattice Ising model is one of the models to show a phase transition.

XY (D=2) model: In the XY model, the Hamiltonian of two interacting particles can be written as-

$$H = -J \sum_{nn} (S_{ix} S_{jx} + S_{iy} S_{jy}) \qquad (1.11)$$

The *z*-component of spins coupling is less with respect to x, and y component so that the spins can confine to rotate in the plane [44] The Mermin-Wagner's theorem for two dimensions displayed that continuous symmetry cannot be broken spontaneously at any finite temperature that suggests no ordered phase at low temperature.

Heisenberg (D=3) model: The Heisenberg model is the extension of the Ising and XY model in 3-dimensional space. The Hamiltonian of interacting spin is as

$$H = -J \sum_{nn} (S_{ix} S_{jx} + S_{iy} S_{jy} + S_{iz} S_{jz}) \qquad (1.12)$$

Here S_i, and S_j are the spin of two interacting particles. The spin retains O(3) symmetry and can point along any direction on the three–dimensional sphere. This system is applicable to isotropic magnetic systems.

1.6. Most Researched Geometrical Frustrated Compounds

Geometrical frustration has been extensively studied in jarosite and in transition metal hydroxyhalogenide compound $M_2(OH)_3Cl$ (where M = *d* electron transition metal magnetic ions, like Cu^{2+}, Ni^{2+}, Co^{2+}, Fe^{2+}, and Mn^{2+}; and X = halogen ions like Cl^-, F^-, and Br^-, etc). A short overview of some of the developments in these model materials would be discussed here.

1.6.1. Jarosite compounds

The Jarosite exhibit the common name of an extensive family of compounds of the form $AB_3(OH)_6(SO_4)_2$, where A^+ = Na, K, Rb, NH_4, H_3O, Ag, Tl, and B^{3+} = Fe, Cr, V. They are the most studied family of kagome lattice antiferromagnets and is related to geometrical frustration and novel magnetism ranging from classical (S = 5/2) to quantum (S = 3/1, 1) limit [7]. The crystal structure of jarosite composed of kagome planes of magnetically active ions (B^{3+}) is bound together by SO_4 tetrahedral units as well as interstitial A^+ ions, as presented in Fig. 1.7. The large variety of compounds would be available by substitution of both the A and B sites leads to a library of possible structures that have been found to display a range of both conventional long-range magnetic order and more exotic unconventional orderings that are summarized in Table 1.2.

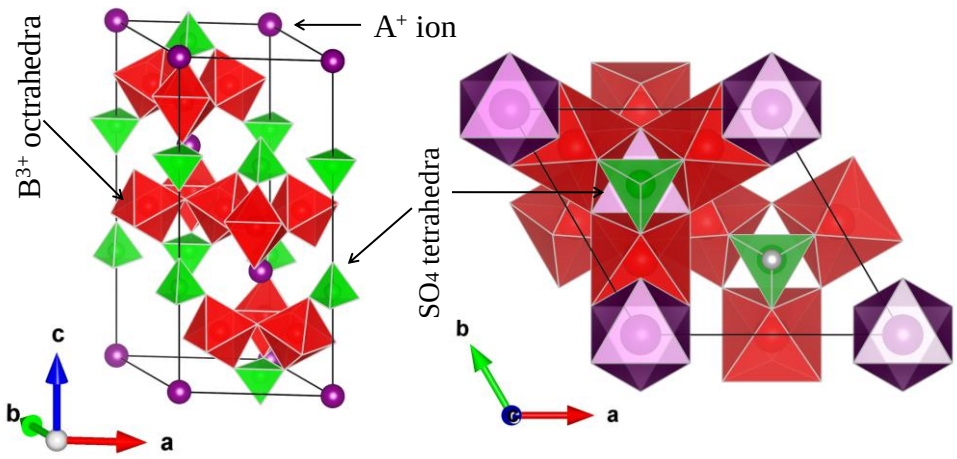

Figure 1.7. Typical crystal structure of jarosite $AB_3(OH)_6(SO_4)_2$, which crystallizes mostly into R-3*m* cell settings displayed in *a*-*c* and *a*-*b* plane. The violet sphere represents the divalent diamagnetic ion.

Table 1.2. Summary of different types of orderings found in the jarosites.

Formula	θ (K)	T_C (K)	Ordering	References
$NaFe_3(OH)_6(SO_4)_2$	-825	61	k = 003/2, q = 0	[45]
$KFe_3(OH)_6(SO_4)_2$	-828	65	k = 003/2, q = 0	[46]
$AgFe_3(OD)_6(SO_4)_2$	-677	51	k = 003/2, q = 0	[7]
$KCr_3(OH)_6(SO_4)_2$	-70	1.8	k = 000, q = 0	[47]
$NaV_3(OH)_6(SO_4)_2$	+52	33	k = 003/2, q = 0	[48]

The most studied classical S = 5/2 spin Fe-jarosite crystallizes into R-3m hexagonal structure shows a magnetically ordered state at low temperature into 120° spin system q = 0 magnetic structure arises due to the propagation of triangular motif with the spin chirality = +1 [7,49]. The observation of this in-plane structure, as opposed to the $\sqrt{3} \times \sqrt{3}$ structure predicted to be stabilized by quantum fluctuations and linear spin-wave theory [50-51]. Spin wave measurements on a single crystal indicate that the Dzyaloshinski–Moriya (D-M) interactions may be the dominant anisotropic interaction in $KFe_3(SO4)_2(OH)_6$ [52-53]. The extensively studied semi-classical S = 3/2 spin $KCr_3(OH)_6(SO_4)_2$ jarosite is kagome antiferromagnet having magnetic transition ranging from 1.5–4 K [47, 54] depending on the crystal growth conditions. Neel order is still the dominant ground-state among the materials, but reduced saturation magnetizations have been seen, indicating strong quantum fluctuations [47]. The Rb^+, NH^+_4 , Na^+ analogous show similar behavior, though a small hysteresis in the magnetization at 2 K is indicative of a small ferromagnetic component, proposed to result from a canting of the 120° spin structure [55]. Long-range ordering still is absent in the hydronium Cr jarosite $(H_3O)Cr_3(SO_4)_2(OH)_6$, similar to Fe jarosite. Quantum fluctuations are seen to suppress long-range order down to 2.2 K, where only 5.4 % of the expected magnetic entropy is recovered [56].

1.6.2. Geometrically Frustrated Transition Metal Hydroxyhalogenide $M_2(OH)_3Cl$ compounds

Since unconventional magnetic transitions have already been reported in the transition metal hydroxyhalogenide series of deformed pyrochlore compound $M_2(OH)_3Cl$, most of these compounds found originally in nature. These materials categories represent a complete series for spin ranging from S = 1/2 to S = 5/2. A brief description of each spin system has been discussed here to understand the magnetism inside this series.

S = 1/2 (Cu^{2+}) spin $Cu_2(OH)_3Cl$

The atacamite is halide mineral exhibit three polymorph like clinoatacamite, botallackite, and paratacamite, which are orthorhombic, monoclinic, and hexagonal structure, respectively as depicted in Fig. 1.8 (a-c).

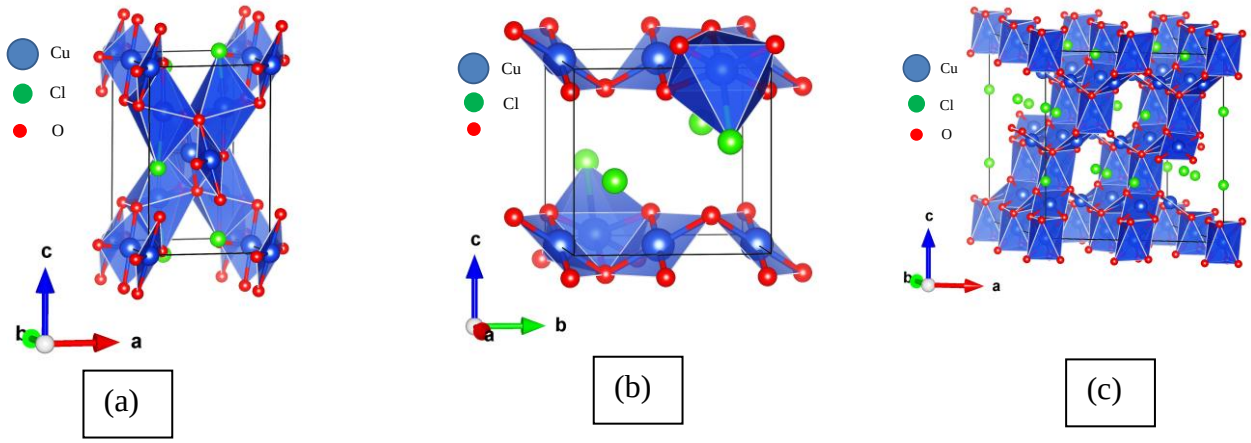

Figure 1.8. Polymorph of $Cu_2(OH)_3Cl$ mineral; (a) atacamite crystallizes into Pnma space group (No.62), (b) botallackite crystallizes into $P2_1/m$ space group (No. 11), and (c) paratacamite crystallizes into R-3 space group (No.148). Reproduce from [57-59].

Antiferromagnetic order with transition temperature T_N = 9.0 K and T_N = 7.2 K has been found in atacamite and botallackite crystal [60-61]. Moreover, the mineral clinoatacamite $Cu_2(OH)_3Cl$ [62] has been found to display antiferromagnetic transition by T_N = 18.1 K along with small entropy fall (0.05Rln2). The disordered spin glass-like state revealed as the temperature-dependent susceptibility curve displayed an anomaly peak at around 6.2 K. The unusual transition in the clinoatacamite $Cu_2(OH)_3Cl$ makes this quantum spin S = 1/2 (Cu^{2+}) a playground to understand the geometrical frustration.

S = 1 (Ni^{2+}) spin $Ni_2(OH)_3Cl$

The S = 1 spin $Ni_2(OH)_3Cl$ compound crystallized in atacamite structure that has been found to demonstrate strong geometrical frustration with antiferromagnetic order with transition temperature below T_N = 4 K **[**63**].** Long-range order confirmed by neutron powder diffraction measurement, whether muon spin relaxation (μSR) experiment confirmed no ordering signature. The anomaly arises from neutron diffraction, and the muon spin relaxation (μSR) experiment of $Ni_2(OH)_3Cl$ has explained according to the antiferromagnetic orders on the frustrated tetrahedral lattice as proposed by Tsuneishi et al. [64] in which the squared Fourier amplitude orders but the amplitude itself fast fluctuating.

S = 3/2 spin $Co_2(OH)_3Cl$

Recently, S = 3/2 spin $Co_2(OH)_3Cl$ compound has found to crystallize hexagonally shows ferromagnetic transition with Curie-Weiss temperature θ_{CW} = 7.8 K [65]. The susceptibility under Zero filled cooled (ZFC), and field-cooled (FC) condition divert below T_C ~ 10 K, which indicates the coexistence of glassiness. Neutron diffraction measurement of $Co_2(OH)_3Cl$ has estimated the possible magnetic structure in which spins on the triangular plane are ferromagnetically ordered. Those on the kagome plane are disordered shown in Fig 1.9.

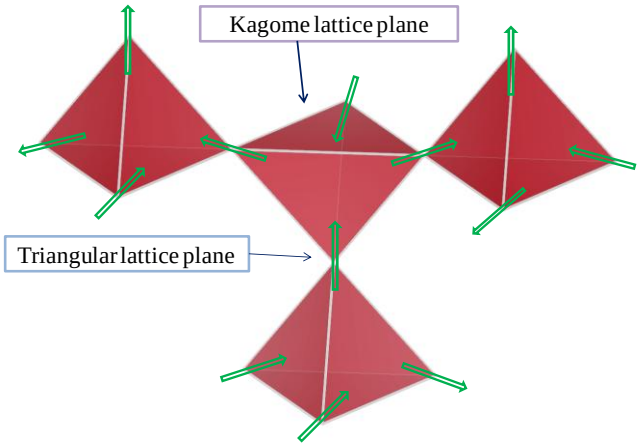

Figure 1.9. Possible magnetic structure of $Co_2(OH)_3Cl$ in which the direction of the spin on the triangular lattice and kagome lattice plane is displayed. Reproduced from [65].

S = 2 spin $Fe_2(OH)_3Cl$

The deformed pyrochlore compound $Fe_2(OH)_3Cl$ that was crystallized in rhombohedral structure, displayed antiferromagnetic transition with T_N = 8.5K along with strong frustration [66]. The neutron diffraction experiment confirmed long-range antiferromagnetic order below T_N = 9.0 K, whereas the proposed magnetic structure depicted in Fig. 1.10 suggests that out of the four Fe^{2+} spins on a tetrahedron, the one spin on the triangular lattice plane is disordered while the other three spins on the kagome lattice plane have frozen moments. The magnetic phase separation and the spin fluctuations coexist with the long-range order makes S = 2 spin system interesting for understanding the magnetism in it.

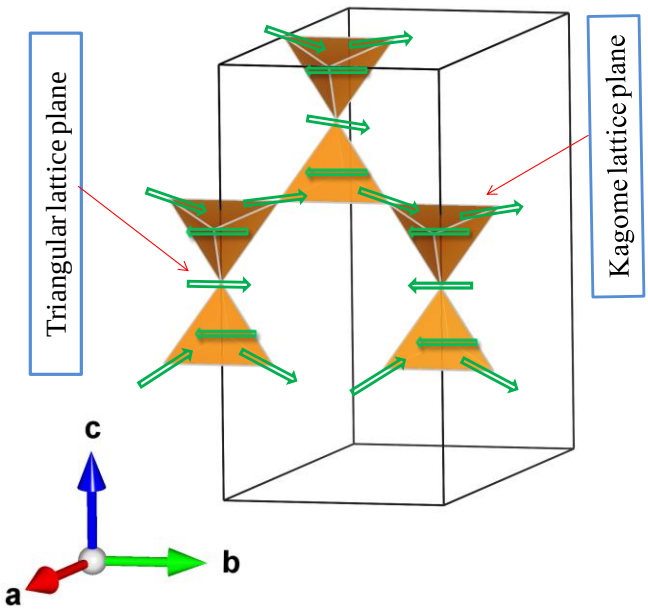

Figure 1.10. Proposed magnetic structure of $Fe_2(OH)_3Cl$ as derived from neutron powder diffraction data in which spins on the kagome plane exhibit frozen moment whereas disordered in a triangular plane. Reproduced from [66].

S = 5/2 spin $Mn_2Cl(OH)_3$

The *S* = 5/2 spin atacamite $Mn_2Cl(OH)_3$ is the end member of $M_2(OH)_3X$ material family crystallized with orthorhombic structure provides Curie-Weiss temperature (θ_{CW}) of -57.8 K. [67]. The effective magnetic moment per Mn^{2+} spin was estimated to be 5.42 μB, which is slightly smaller than the expected value of free Mn^{2+} ion suggests the result of the crystal field's influence. Moreover, glassiness nature below 2.7 K confirmed by zero field cool (ZFC) and field cool (FC) measurement. The specific heat measurement for $Mn_2(OH)_3Cl$ confirmed two successive phase transitions at 3.4 K and 2.7 K, respectively, where the two peak positions slightly decrease in the applied magnetic field, supporting antiferromagnetic transition.

1.7. Experimental Search of Spin Liquid

In order to understand the geometrical frustration, kagome lattice antiferromagnets (KLA) are suitable candidates because of having four coordination numbers with respect to six coordination numbers in the triangular lattice [68]. Moreover, the kagome lattice compound has higher degeneracy with respect to 2D-triangular lattice compound and pyrochlore crystal, as discussed earlier. The search for quantum disorder ground state in two dimensional systems has been challenging to us. The doping of non magnetic ions in the 3D-deformed pyrochlore lattice [e.g. clinoatacamite $Cu_2(OH)_3Cl$] will lead to 2D-vortex sharing kagome lattice compound of general formula $AM_3(OH)_6X_2$ [where, A = non-magnetic ion, M = transition metal ions, X = halogen ions]. The doped compound consists of one-quarter of the pyrochlore lattice sites are occupied by non-magnetic ion (A^{2+}) and the remaining sites are occupied by magnetic (M^{2+}) ion to form alternate stack layer of kagome lattice plane and triangular lattice plane. Moreover, the magnetic ion (M^{2+}) at the John-Teller distorted O_4Cl_2 octahedra separated by a layer of non-magnetic (A^{2+}) ion in O_6 octahedra. Because of having extensive large degenerate ground state, the kagome lattice geometry is believed to exhibit spin liquid behavior both in quantum and classical limits.

Herbertsmithite $ZnCu_3(OH)_6Cl_2$ is the most researched S = 1/2 spin diamagnetic (Zn^{2+}) ion substitute end member (x = 1) of atacamite family $Cu_4(OH)_6Cl_2$ [4-5]. The substitution of Zn^{2+} ion in the pyrochlore lattice results in kagome lattice S = 1/2 Cu^{2+} antiferromagnets in which kagome lattice plane stack on triangular lattice alternatively, as displayed in Fig 1.11.

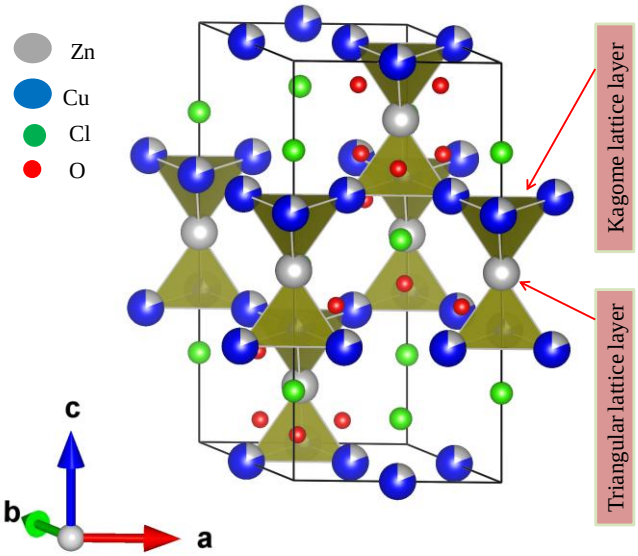

Figure 1.11. Crystal structure of herbertsmithite in which kagome and triangular lattice stack alternately that has grown by selectively substitution of Zn^{2+} ion in their parent pyrochlore type lattice. Reproduced from [69].

Macroscopic ground state degeneracy of the theoretical kagome lattice has been found in herbertsmithite which lead to much purer kagome physics. Temperature-dependent susceptibility measurements displays absence of ordered ground state down to 2 K, while muon spin relaxation (μSR) and specific measurement extend this limit to 50 mK [4,70]. The intersite mixing of Cu^{2+} and Zn^{2+} ion in kagome and triangular plane confirmed by neutron diffraction, ^{17}O-NMR, and susceptibility measurements [71-73], which introduce a 3-dimensional exchange pathway in the kagome to triangular lattice plane. Moreover, electron spin resonance (ESR) measurements have shown a significant antisymmetric Dzyaloshinsky-Moriya (DM) component in the exchange

Hamiltonian [74]. Herbertsmithite is treated as the first practical quantum kagome antiferromagnet which displays spin liquid state.

A polymorph of Herbertsmithite called Kapellasite $ZnCu_3(OH)_6Cl_2$ [75] that crystallizes with space group P-3*m*1 also contains kagome network displayed gapless spin liquid which offers unusual dynamic short-range correlations that persist down to 20 mK. Since many theoretical and experimental works have already been done on $S = 1/2$ kagome antiferromagnet, there are many unanswered questions still unclear regarding the intrinsic ground state of this spin system.

The $S = 3/2$ kagome antiferromagnets $MgCo_3(OH)_6Cl_2$ and $ZnCo_3(OH)_6Cl_2$ [76-77] were successfully synthesized by substituting Mg^{2+} and Zn^{2+} ions in the triangular planes of its parent compound $Co_2(OH)_3Cl$. The intersite mixing of Mg^{2+} and Co^{2+}; Zn^{2+} and Co^{2+} in $MgCo_3(OH)_6Cl_2$, and $ZnCo_3(OH)_6Cl_2$, respectively, showed similar inter-site mixing of Zn^{2+} and Cu^{2+} in herberthsmithite. The $MgCo_3(OH)_6Cl_2$ and $ZnCo_3(OH)_6Cl_2$ compound crystallized in hexagonal structure with R-3*m* symmetry; both showed short-range correlations with persistent spin fluctuations in the vicinity of the ordered state below $T = 2.7$ K.

The $S = 2$ spin quasi-classical kagome antiferromagnet $MgFe_3(OH)_6Cl_2$ [6] has synthesized by solvothermal reaction whose crystal structure is similar to most researched kagome lattice herberthsmithite $ZnCu_3(OH)_6Cl_2$ in which kagome plane and triangular plane stack in one another in the *c*-axis direction. The substitution of non-magnetic Mg^{2+} ion into its mother compound $Fe_2(OH)_3Cl$ converts the compound from 3D to 2D materials. Antiferromagnetic order with transition temperature 9.9 K was observed, which reduces the frustration in comparison to its mother compound $Fe_2(OH)_3Cl$, which exhibit transition temperature by $T_N = 8.5$ K. Long-range Heisenberg-like spin order was found to develop in this compound as revealed by neutron powder diffraction experiment, whereas parent compound $Fe_2(OH)_3Cl$ displayed antiferromagnetic order along with spin fluctuation. The spin moment of Fe^{2+} ion, as depicted in Fig 1.12 confined in the kagome plane with spin vector chirality -1 by 120º spin steps. The $S = 2$ spin $MgFe_3(OH)_6Cl_2$ is treated as a real system with a quasi-classical

Heisenberg spin that is considered as a reference system for quantum Heisenberg kagome antiferromagnets.

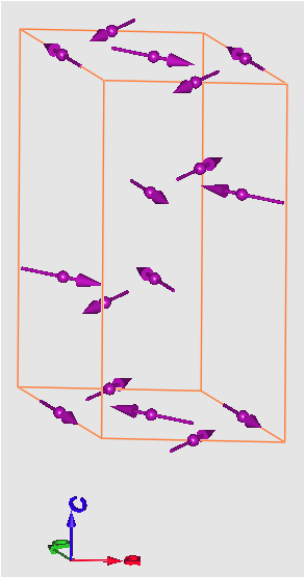

Figure. 1.12: Proposed magnetic structure of $MgFe_3(OD)_6Cl_2$ derived from neutron powder diffraction data which confirmed the spin confined in the kagome plane with spin vector chirality -1 by 120º spin steps. Reproduce from [6].

The spin liquid could be quantum spin liquid (QSL) and classical spin liquid (CSL) depending on the spin moment's value. The above discussion evident that quantum spin liquid (QSL), short-range correlations with persistent spin fluctuation, and long-range order (LRO) have been found in $ZnCu_3(OH)_6Cl_2$, $MgCo_3(OH)_6Cl_2$, and $MgFe_3(OH)_6Cl_2$ compound, respectively. There is a tendency from spin liquid to long-range order (LRO) with an increased magnetic moment. This observation is also supported by Merino et al. [78] 's theoretical report regarding the rapid diminishing of quantum fluctuation with increasing the spin moment of honeycomb lattices.

Almost all theoretical studies predicted an extremely high degeneracy of the ground states for a classical spin kagome antiferromagnet even at low temperatures. But experiential observation on classical spin kagome lattice provides spin liquid to long-range ordered (LRO)

state. Therefore, the classical spin kagome lattice's ground state has received intense interest to explore the unexpected LRO. The possible reason behind the unexpected long-range order (LRO) in the classical kagome lattice might be the followings-

First, the q = 0 long-range order (LRO) with positive spin chirality at a high T_N up to 65 K has already reported in the S = 5⁄2 kagome antiferromagnetic jarosite, i.e., in potassium jarosite $KFe_3(OH)_6(SO_4)_2$, plumbojarosite $Pb_{0.5}Fe_3(OH)_6(SO_4)_2$, and argentojarosite $AgFe_3(OH)_6(SO_4)_2$, etc.[7,49,79]. The unexpected LRO might be arises in the spin system due to the presence of non-magnetic defects and weak ion anisotropy [49, 79]. Experimental evidence suggested an Ising nature for the jarosite compounds.

Second, the Dzyaloshinskii-Moriya interaction (DMI) as portrayed in Fig. 1.13 arises from the interplay of spin-orbit interaction and super-exchange interaction [80] acting between the excited state of one ion and the ground state of the other ion, which results in spin canting by a small angle. This interaction is usually found in antiferromagnets, resulting in a small ferromagnetic component perpendicular to the spin-axis of the antiferromagnets.

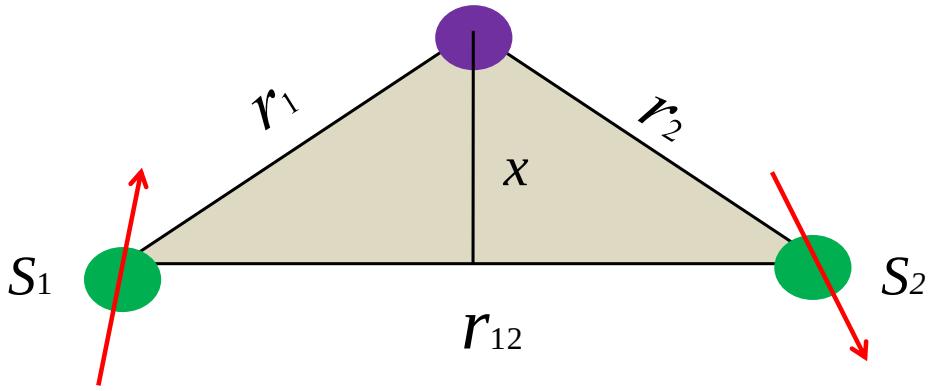

Figure 1.13. The schematic view of spin canting between two magnetic ions allowing small ferromagnetism results Dzyaloshinskii–Moriya interaction (DMI).

The infinitesimally small Dzyaloshinskii-Moriya interaction (DMI) in the classical kagome lattice favors long-range order with q = 0 phase all-in all-out structure with 120º spin steps [81].

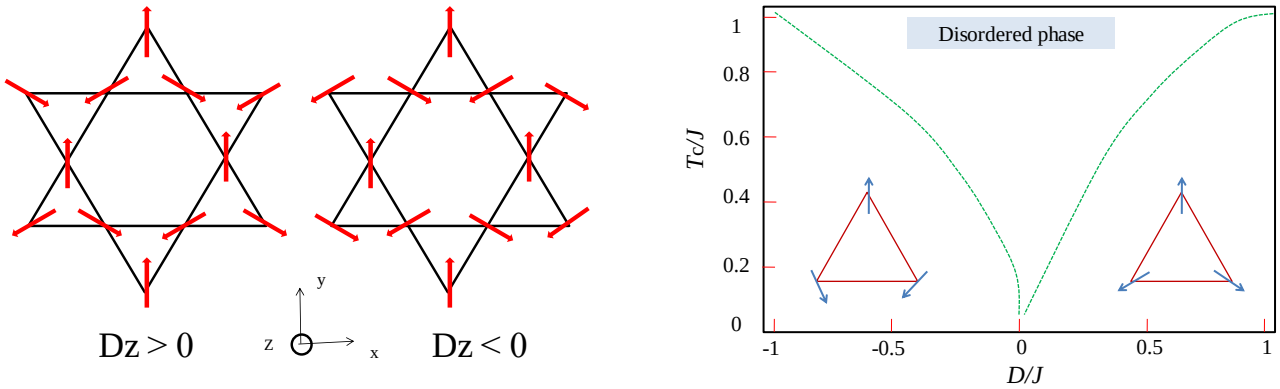

Figure 1.14. (a) D vector is perpendicular to the kagome plane. The spins lie in the kagome plane, whether the sign of D_z selects the chirality, (b) the critical temperature as a function of D/J in the kagome plane represents the coplanar q=0 low-temperature magnetic structures. Reproduced from [81].

The q = 0 structure exhibit two chirality depending on the vector D_z sign as represented in Fig 1.14 (a). In order to study the behavior of this system at finite temperature, Monte Carlo simulations have been performed on finite-size clusters with classical Heisenberg spins. The behavior of the critical temperature with respect to D/J is plotted in Fig. 1.14(b). At D = 0 in Fig. 1.14 (b) corresponds to classical kagome lattice along with antiferromagnetic nearest neighbor (*nn*) exchange interactions. This system exhibits partial order, and the coplanar states are asymptotically selected as the temperature is lowered [82] (order by disorder). However, as soon as D has reached finite value, a phase transition occurs at finite temperature. The low-temperature magnetic structure will be governed by DMI in the studied system. The critical temperature is almost linear in D, and only weakly dependent on the strength of the antiferromagnetic exchange interactions (J). Therefore, DMI has a first-order effect on a

degenerate ground state, while usually, DMI acts as a small perturbation on the antiferromagnetically ordered ground state, leading to second-order corrections. Moreover, the unexpected long-range order (LRO) found in jarosites has been predicted to arise due to the Dzyaloshinskii-Moriya interaction (DMI) [52-53].

Third, the unexpected long-range ordering can also be explained by the theoretical dipolar + Heisenberg interaction model proposed by Maksymenko et al**.**[83-84] that predicted a three-sublattice long-range order with a coplanar 120º spin structure.

The formula can calculate the exchange interaction J_e-

$$J_e = \frac{3k_B\theta_{CW}}{2zJ(J+1)} \qquad (1.13)$$

where, k_B = Boltzman's constant, θ_{CW} = Curie-Weiss temperature, z = number of nearest neighbour (z = 4, for kagome lattice compounds), and J = L + S = total angular momentum.

The dipolar interaction energy (D) is calculated as-

$$D = \frac{\mu_o}{4\pi}\frac{\mu^2}{R_{nn}^3} \qquad (1.14)$$

where, R_{nn} = nearest neighbor distance, and μ = magnetic moment of the atoms in the compound.

Extensive ground state degeneracy would be lifted when the ration of D/J_e lies between $0 < D/J_e < 5.67$, which results in three sub-lattices long-range 120 º orders Heisenberg spin confined in the kagome plane.

Moreover, extensive degeneracy without long-range order has been found in the first-neighbor Heisenberg antiferromagnet on the kagome lattice even at T = 0 [82. 85]. A second-neighbor Heisenberg coupling J_2 leads to a q = 0 Néel order for J_2 > 0 (antiferromagnetic interactions) or a $q = \sqrt{3} + \sqrt{3}$ order for J_2 < 0 (ferromagnetic interactions) near T = 0 [86]. Extension of the $J_1 - J_2$ model to ferromagnetic nearest-neighbor coupling (J_1 < 0) leads to a Néel long-range order near T = 0 for $J_2 \geq -J_1/3$ with 12 noncoplanar sublattices and

incommensurate noncoplanar structures for $J_2 < -J_1/3$ [87]. More recently, the interplay of dipolar interactions and geometrical frustration has been discussed, and long-range ordering has been shown to be stabilized by consideration of both dipolar and nearest-neighbor interactions [83-84]. Conversely, the classical model for an Ising kagome antiferromagnet remains disordered even at $T = 0$ [88-89]. A more recent Monte Carlo simulation study has predicted long-range order for the classical dipolar Ising kagome antiferromagnet [90]. While the quantum fluctuations for a Heisenberg kagome antiferromagnet can lift the degeneracy and lead to order from the disorder at $T = 0$ [50]**,** they fail to induce a magnetic order the Ising model at any temperature [91-92]. Despite these advancements, it is clear that the nature of the classical spin kagome at low-temperature states for both Heisenberg and Ising kagome antiferromagnets remains largely unknown.

1.8. Motivation of the Present Research

The theoretical studies predicted an extremely high degeneracy of the ground states for a classical spin kagome antiferromagnet even at $T = 0$. In the case of quantum spin system $S = 1/2$, there is a good agreement between the theoretical prediction and experimental observation. But, there is a large discrepancy between theoretical prediction and experimental result for the classical kagome antiferromagnets as compared to the quantum spin kagome system. The $S = 5/2$ spin kagome antiferromagnet $MgMn_3(OH)_6Cl_2$ is the end member of Mg^{2+} ion substituted deformed pyrochlore $Mn_2(OH)_3Cl$ whose ground state is of considerable interest both as a classical kagome antiferromagnet as well as a reference system for the spin liquid kagome antiferromagnets $ZnCu_3(OH)_6Cl_2$/$MgCu_3(OH)_6Cl_2$. Therefore, the present research's specific objective is to explore the ground state of $S = 5/2$ classical spin kagome antiferromagnet $MgMn_3(OH)_6Cl_2$. In order to realize this objective, the author would like to synthesize polycrystalline $Mg_xMn_{4-x}(OH)_6Cl_2$ compound by solvothermal reaction process and allow the compounds for x-ray diffraction experiment, magnetic measurements, and neutron powder diffraction experiments.

1.9. Thesis Layout

The present chapter discusses the magnetism and geometrical frustration in solids along with few exotic states like spin glass, spin liquid, etc. A brief literature review has been discussed, which will lead us to find the present research work's objective.

In the chapter-2, the experimental techniques that have been utilized to characterize the presently studied materials would be reviewed briefly. Among them, x-ray diffraction (XRD) technique, temperature depended on the magnetic measurement technique, and neutron powder diffraction technique is essential. A special emphasis would be given on magnetic measurement by Magnetic property measurement system (MPMS) based on Superconducting Quantum Interface Devices (SQUID) as well as on Time of Flight (TOF) neutron diffraction technique. Since the Rietveld refinement procedure generally refines the scattering data, a brief and clear idea on Rietveld based refinement will be intended to add in this chapter. Moreover, a brief discussion of simulated annealing representation analysis (SARAh) will be reviewed for estimating the proposed magnetic structure.

In chapter-3, the synthesis and magnetism of S = 5/2 (Mn^{2+}) spin kagome lattice antiferromagnet $Mg_xMn_{4-x}(OH)_6Cl_2$ has been discussed briefly. A clear and easy description of the compound synthesis and their characterization has been added here. The $Mg_xMn_{4-x}(OH)_6Cl_2$ compound's structural and magnetic measurements have added along with the results of the neutron diffraction experiment to find the crystal structure and proposed magnetic structure of $MgMn_3(OD)_6Cl_2$ compound.

Chapter-4 intends to conclude the present research works and suggested future work to put forward the present research.

Chapter-2

Experimental Methods

Different experimental techniques have been employed to explore the phase and magnetic characteristics of the geometrically frustrated compound, like x-ray diffraction (XRD), neutron powder diffraction technique, and magnetic property measurement technique based on superconducting quantum interface device (SQUID). Here, a brief description of the used experimental methods are given in the followings-

2.1. Structural Characterization by X-ray Diffraction Technique

The scattering technique is extensively employed to investigate the detailed structure of materials using energetic particles. Particle-materials interactions could be elastic or inelastic scattering whether incident particles' energy is equal to the scattered particles or unequal to each other, respectively. The most extensively used scattering techniques are x-ray diffraction (XRD) technique, neutron diffraction technique, and electron diffraction technique. The latter one is suitable to investigate gas-phase structures of compounds with sufficient volatility and molecular simplicity. In the present research, x-ray diffraction (XRD) would initially be employed to characterize the compound's structure. The x-ray diffraction technique is based on Bragg's law, which is briefly described here.

2.1.1. Bragg's Law of X-ray Diffraction

The wavelength of x-ray (~10^{-10} – 10^{-11} m) is comparable to the interplanar distance (d_{hkl}) of the crystal lattice in which the atoms are arranged periodically. The incident x-ray is scattered from the atoms that are residing on the crystal lattice plane giving rise to constructive interference when the path difference between the scattered and incident x-ray is an integral multiple of wavelength. The geometrical illustration of Bragg's law is presented in Fig. 2.1 giving the formula below [27]-

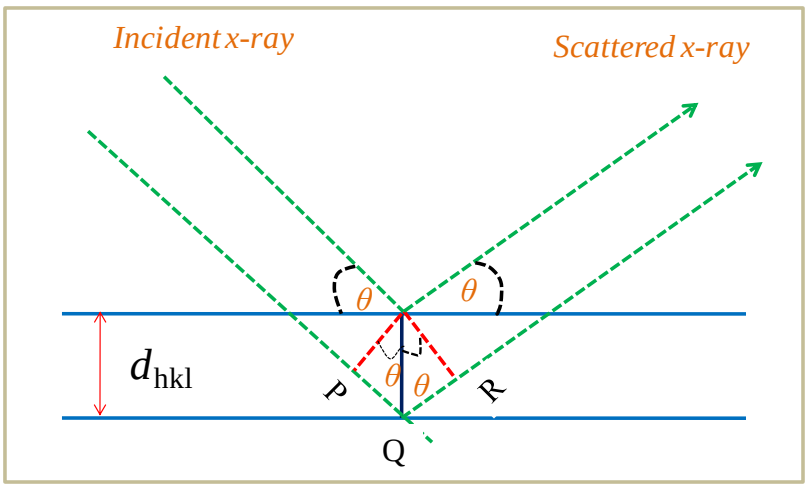

Figure 2.1. Bragg's law in which incident x-ray is scattered from crystal lattice giving rise to constructive interference.

$$n\lambda = PQ + QR = 2d_{hkl}\sin\theta \qquad (2.1)$$

Here, integer 'n' in the order of reflection, λ is the wavelength of x-ray, and θ is the angle between the incident beam and the normal to the reflecting lattice plane. By measuring θ, the interplanar spacing of the crystal can be determined as (for cubic crystal system)-

$$d_{hkl} = \frac{a}{\sqrt{h^2 + k^2 + l^2}} \qquad (2.2)$$

Here, *hkl* are Miller indices. In order to identify an unknown crystal structure, the powder diffraction pattern is recorded with the help of a diffractometer, and a list of *d*-value and the relative intensities of the diffraction line is prepared. These data are compared with the standard line pattern available for various compounds in the powder diffraction file (PDF) database.

In the present research, X-ray diffraction facilities of the Analytical Research Center for Experimental Sciences of Saga University, which used Cu *Kα* (λ=1.5406Å) source has been used for structural characterization. The x-ray data was measured from 10 to 65° at 1 deg./mins in

continuous mode. The x-ray data was refined by the Rietveld refinement process with the calculated data.

2.2. Neutron Powder Diffraction

Neutron diffraction utilized the concept of neutron scattering to determine the atomic and/or magnetic structure of the materials. Because of the neutron's different scattering properties compared to x-ray, complementary information can be obtained from neutron diffraction. More specifically, the accurate position of light atoms such as hydrogen, deuterium, or lithium can easily be understood by neutron diffraction.

Since neutron has a magnetic moment that can easily interact with the magnetic moments found within a material that results in magnetic scattering that is superimposed upon the nuclear scattering in any magnetic material. A sample to be examined is placed in a beam of thermal, hot or cold neutrons to obtain a diffraction pattern that provides information of the structure of the material. The measurement principle of neutron diffraction is based on the Bragg's equation similar to x-ray diffraction.

2.2.1. Nuclear Bragg scattering

Nuclear Bragg diffraction occurs from planes in a crystal separated by a distance *d*, as shown in Fig 2.2 (a). The scattering system can be defined as having a dimension (in direct space):

$$\boldsymbol{r} = n_1\boldsymbol{a} + n_2\boldsymbol{b} + n_3\boldsymbol{c} \qquad (2.3)$$

The incoming neutrons are considered as plane waves with wavelength of $= \frac{2\pi}{|k|}$, where $k_i = k_f = |k|$ wave number. The form of Bragg's law in case of neutron diffraction would be similar to Eq. (2.1) as for X-ray diffraction.

The reciprocal lattice that is displayed in Fig. 2.2(b) can be defined with respect to the direct space lattice as:

$$\boldsymbol{a}^* = \frac{2\pi}{v_0}\boldsymbol{b}\times\boldsymbol{c},\ \boldsymbol{b}^* = \frac{2\pi}{v_0}\boldsymbol{c}\times\boldsymbol{a},\ \boldsymbol{c}^* = \frac{2\pi}{v_0}\boldsymbol{a}\times\boldsymbol{b} \qquad (2.4)$$

where ***a, b*** and ***c*** are unit vectors of the nuclear cell and v_0 is the volume of the unit cell whose value as $v_0 = \boldsymbol{a}.(\boldsymbol{b} \times \boldsymbol{c})$. The direct lattice and the reciprocal lattice are related as a Fourier transform pair.

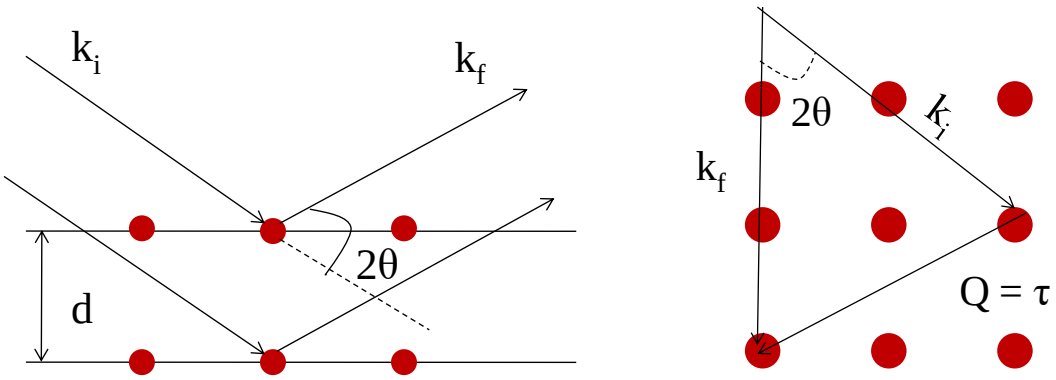

(a) (b)

Figure 2.2. (a) Nuclear Bragg's diffraction in which incoming neutrons scattered from the nuclei within the crystal lattice, (b) representation of reciprocal space of crystal.

In order to observe scattering, the scattering vector Q must be equal to a reciprocal lattice vector τ (i.e. $Q = k_i - k_f = \tau$) [93]. The intensity of the elastically scattered neutrons is given by:

$$\left(\frac{d\sigma}{d\Omega}\right)_{nuc} = N\left(\frac{2\pi}{v_0}\right)^3 \sum_{\tau} \delta(Q-\tau)|F_N(Q)|^2 \qquad (2.5)$$

where, N is the number of unit cells and F_N is known as the structure factor. So for a particular material, $I_N \propto |F_N(Q)|^2$. The structure factor is given by:

$$F_N(Q) = \sum_j b_j \exp(2\pi i \boldsymbol{Q}.\boldsymbol{r}_j) \exp(-W_j) \qquad (2.6)$$

where the sum is over all j atoms and $\exp(-W_j)$ is the Debye-Waller factor, which takes into account the thermal motion of the atom.

In scattering systems, there is a variable scattering length at different sites due to nuclear spins or isotopes. This results in the cross-section being separated into coherent and incoherent terms.

Coherent scattering depends on the correlation between the same nucleus' positions at different times and on correlations of different nuclei at different times. The result is interference effects. It also depends on the average scattering length, assuming no correlation between positions and scattering length. The coherent scattering is observed as intensity or Bragg peaks. They are either given as a function of 2θ, Q or d. These are related by:

$$Q = \frac{2\pi}{d} = \frac{4\pi sin\theta}{\lambda} \qquad (2.7)$$

Incoherent scattering depends only on the correlation of the same nucleus' positions at different times, which does not give rise to interference effects. The incoherent scattering is due to the random distribution of deviations of the mean value's scattering lengths.

2.2.2. Magnetic Scattering

The total scattering from a sample as a Q's function by considering the magnetic scattering is given as the sum of nuclear and magnetic components:

$$\frac{d\sigma}{d\Omega_{tot}} = \frac{d\sigma}{d\Omega_{nuc}} + \frac{d\sigma}{d\Omega_{mag}} \qquad (2.8)$$

$\frac{d\sigma}{d\Omega_{mag}}$ has the same form as Eq. 2.5 but now k is introduced to describe the magnetic order.

$$(\frac{d\sigma}{d\Omega})_{mag} = N(\frac{2\pi}{v_0})^3 \sum_\tau \sum_k \delta\,(Q - \tau - k)|F_M(Q)|^2 \qquad (2.9)$$

k is known as the propagation vector of the magnetic structure or *k*-vector. At *k* =(0, 0, 0), the magnetic and nuclear Bragg peaks will lie on top of each other; whereas magnetic peaks appear at different positions to the nuclear peaks when $k \neq (0, 0, 0)$. For magnetic scattering from a particular system $I_M \propto |F_M(Q)|^2$ where $F_M(Q)$ is given by:

$$F_M(Q) = F(Q) \sum_j m_{\perp_j} \exp(2\pi i \boldsymbol{Q}.\boldsymbol{r_j}) \qquad (2.10)$$

$m_{\perp_j}$ is the magnetic component of the ordered moment perpendicular to *Q* on the jth atom in the unit cell, and *F*(Q) is known as the magnetic form factor. The magnetic form factor arises due to the magnetic moment being spread out over an atom. The form factor is present for all magnetic systems regardless of the presence of magnetic ordering or otherwise.

Neutron diffraction can be categorized into elastic and inelastic scattering depending on the incident's energy and momentum and scattered neutrons. Now a day's constant wavelength and time of flight (TOF) neutron diffraction technique have been widely used.

2.2.3. Time of Flight Neutron (TOF) Diffraction Technique

Time of flight (TOF) neutron powder diffraction technique is treated as one of the standard techniques used for crystal and magnetic structure determination of polycrystalline materials with pulsed neutron sources [94]. The TOF diffractometer operates differently than constant wavelength (CW) diffractometer based on the standard Debye - Scherrer method. The Debye - Scherrer method for neutron was first developed and employed in the 1940's [95]. Instead of measuring Bragg's reflection by scanning a detector from low to high 2θ scattering angles, in the TOF technique, a neutron spectrum of scattered neutrons is measured at a constant scattering angle ($2\theta_o$).

In the TOF experiments, the polychromic neutron beam coming from a moderator and scattered at a fixed scattering angle ($2\theta_0$) giving rise to constructive interference expressed by Bragg's law-

$$\lambda_{hkl} = 2d_{\mathrm{hkl}}\mathrm{Sin}\theta_0 \qquad (2.11)$$

where λ_{hkl}, d_{hkl} are neutron wavelength and interplanar distance of the crystal lattice, respectively. The neutron wavelength is determined, according to the de Broglie relation, by the neutron momentum, mV as:

$$\lambda = \frac{h}{mv} = \frac{ht}{mL} \qquad (2.12)$$

where, *h* is the Planck constant, *v* neutron velocity, *m* neutron mass, *L* a flight path, and *t* time of flight.

In time of flight (TOF) neutron diffraction technique, a pulse of neutrons with different wavelengths is produced, and the time elapsed by these neutrons to travels from source to the detector is measured. The neutron will gain or lose energy, resulting in the change of neutron's velocity, which will vary the arrival time of neutrons to the counters.

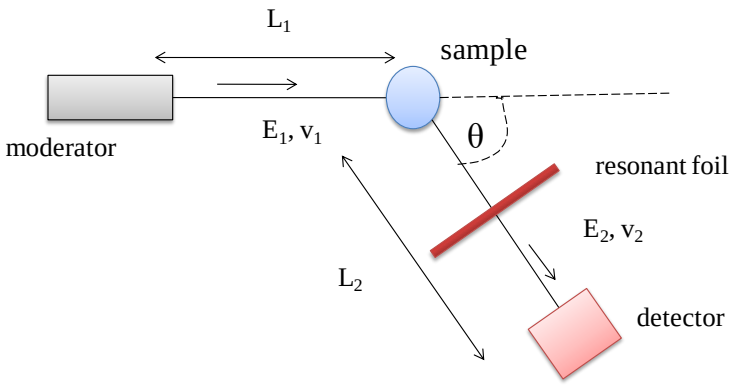

Figure 2.3. Schematic view of the geometry of time of flight (TOF) spectroscopy in which L_1, and L_2 are the distance traversed by incident beam and scattered beam with velocities v_1, and v_2, respectively.

$$t = t_0 + \frac{L_1}{v_1} + \frac{L_1}{v_2} \qquad (2.13)$$

The time of flight (TOF) is related to interplaner distance between two lattice planes (*d)* by the polynomial formula [96] of the following –

$$TOF = t = C_0 + C_1 d + C_2 d^2 + \qquad (2.14)$$

where, C_1 and C_2 are *d*-spacing dependants, and C_0 is *d*-spacing independent parameters. The TOF diffractometer's performance depends on the resolution ($\Delta d/d$), which is a measure of the spread in the Bragg's reflection for a given *d*-spacing. The resolution of TOF pulse source depends on the uncertainty in time (Δt); uncertainty in angular degree ($\Delta\theta$), and uncertainty in flight path (ΔL).

The formula describes the resolution of a TOF diffractometer-

$$\frac{\Delta d}{d} = [(\frac{\Delta t}{t})^2 + (\Delta\theta cot\theta)^2 + (\frac{\Delta L}{L})^2]^{1/2} \qquad (2.15)$$

Since path uncertainties and angular uncertainties are independent of wavelength, the overall geometrical contribution to resolution is nominally constant when the scattering angle is fixed. The main contribution to Δt gives the moderation process of neutrons.

Using the TOF method, it is possible to reach a very high resolution in the diffraction of polycrystalline materials. Nowadays, high-resolution powder diffractometer (HRPD) is the best resolution neutron diffractometer in the world and is designed to achieve an optimal balance between the maximum practical resolution attainable $\Delta d/d$=4–5×10^{-4}[97] and reasonable counting times. In the present research, the time of flight (TOF) neutron diffraction facilities of Super HRPD (BL-08), J-PARC, Japan will be used to perform neutron diffraction experiments. The super HRPD at J-PARC utilizes the H_2 moderator giving a 0.1-0.15%, a 0.4-0.7%, and a 0.7-3.0% resolution for higher-angle, 90-degree, and low-angle banks.

Around 1.7 gm of $MgMn_3(OD)_6Cl_2$ powdered samples were poured into the vanadium cylinder (as shown in Fig. 2.4) in the glove box at the helium atmosphere to prevent surface oxidation. The cylinder was indium sealed and allowed it in the cryostat to reach low temperatures. Neutron powder diffraction at Time of Flight (TOF) mode was carried out at 2.7 K and 20 K temperature.

Table-2.1. Summary of values of C_0, C_1, and C_2 for different data bank in BL-08 (Super HRPD) in J-PARC, Tokai.

Data bank	C_0	C_1	C_2
90º (QA)	-5.075	34468.469	0.140
Higher angle (BS)	-5.407	47651.018	-1.167
Lower angle (LA)	-12.068	11657.862	-3.166

Figure 2.4. Photograph of mounted powder sample in vanadium cylinder for neutron diffraction experiment.

The temperature-dependent measurement was also carried out to find the effect of temperature on the lattice constants. The Time of Flight (TOF) mode neutron diffraction provides data in three different bank namely, backscattered bank (BS) or higher angle bank, lower angle (LA) bank, and 90º bank or QA bank with different values of C_0, C_1, and C_2 parameters as summarized in Table 2.1. The *d*-spacing of the present studied was calculated using the parameters from Table 2.2 which will finally results the scattering vector (Q) using the Eq. (2.7).

2.3. Diffraction Data Analysis by Rietveld Refinement Process

Rietveld refinement as introduced by Hugo Rietveld [98] is a process to characterize crystalline materials using diffraction data collected either by X-ray or neutron diffraction technique. A non-linear least square technique is employed to refine crystal structure by fitting the observed diffraction pattern to the calculated diffraction pattern. It requires few initial approximations of several free parameters, like peak shape parameters, unit cell parameters, background

parameters, and coordinates of all atoms in the crystal structure. Moreover, this technique has been extensively used like *ab* initio crystal structure characterization, indexing, background subtraction, refinement of lattice parameters, refinement of crystal-structure parameters (fractional coordinates, occupancies, and atomic displacement parameters), refinement of magnetic-structure parameters (magnitudes and directions of magnetic moments), correction for preferred orientation, identification of impurity reflections, quantitative analysis of mixtures, determination of integrated intensities, full-widths at half-maximum intensities (FWHM), and peak positions, and determination of crystallite sizes and microstrains, etc.

A lot of Rietveld refinement software packages are currently available, including the freeware programs Reitan-FP [99], GSAS [100], and FullProf [101], Z-Rietveld [102]. The XRD data have been analyzed by the Rietan-FP program, while the neutron powder diffraction data is analyzed by both Z-Rietveld as well as FullProf suite software through this research work.

2.4. Simulate Annealing Representation Analysis (SARAh) for Magnetic Calculation

Relation among magnetic moments of the non-primitive cell was calculated initially by comparing it with a known magnetic structure by trial and error basis. The Group theory argument provides us the easiest and potential way to calculate the symmetry allowed relation between the magnetic moments. The basis vector, which is the result of this calculation, simply describes the possible magnetic structure. The technique that employs Group theory for magnetic structure calculation is termed representation analysis (RA) [103-108]. Representation analysis (RA) is a technique based on the Landau theory of second-order phase transition that is associated with the decomposition of magnetic representation (Γ) of the little Group (G_k) into irreducible representation based on the FORTRAN77 based KAREP program [109].

Recently, a large number of computer-aided software has been used to perform the calculations to complete magnetic symmetry analysis. Irreducible Representations (IR) can be understood using BASIREPS [110], KAREP [109], MODY [111], and SARAh [112]. Simulate annealing

representation analysis (SARAh) program is the combination of simulated annealing (SA), and representation analysis (RA) utilizes non-magnetic space group, and propagation vector (*k*), and atomic positions of the magnetic atoms as applied input parameters creates a powerful latest method for determination of possible magnetic structures. A unique feature of SARA*h* is that refinement is carried out in terms of the basis vector coefficients and so the symmetry of $G_{\boldsymbol{k}}$ is implicitly taken into account.

2.5 Magnetic Property Measurement System (MPMS) Based on SQUID

Superconducting Quantum Interface Device (SQUID) is the most sensitive as well as an effective magnetic property measurement system (MPMS) whose sensitivity range from micro-tesla to picotesla levels [113]. The construction of SQUID based on Josephson effect in which electrical current density through a weak electrical contact between two superconductors, as depicted in Fig 2.5 (a) depends on the phase difference ($\Delta\varphi$) of the two superconducting wave functions. Moreover, the time derivative of $\Delta\varphi$ is correlated with the voltage across this weak contact. In a superconducting ring with one or two weak contacts, $\Delta\varphi$ is additionally influenced by the magnetic flux Φ through the ring.

These types of structures can be used to convert magnetic flux into an electrical voltage. This is the basic working principle of the SQUID magnetometer. The SQUID can be classified into *rf*-SQUID and *dc*-SQUID depending on the number of Josephson junctions. The *dc*-SQUID normally uses two Josephson junction, whether *rf*-SQUID employs a single Josephson junction. Moreover, *dc*-SQUID offers lower noise compared with *rf*-SQUID.

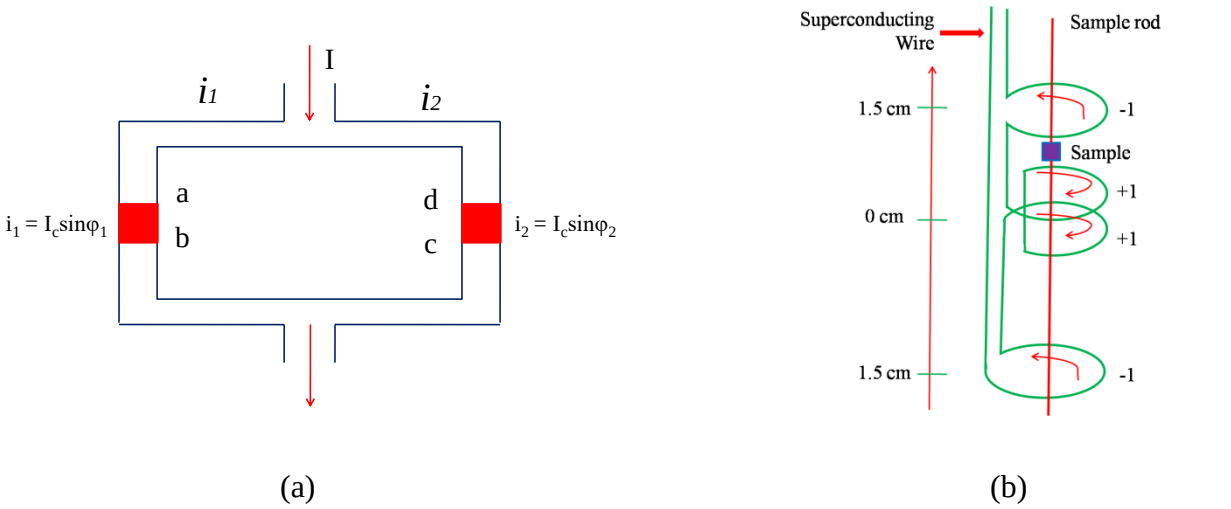

(a) (b)

Figure 2.5. (a) Diagram of a dc SQUID in which current *I* enter and split into the two paths, each with currents i_1 and i_2. The thin barriers on each path are Josephson junctions, which together separate the two superconducting regions. Φ represents the magnetic flux threading the dc SQUID loop, (b) Superconducting loop configuration of the pick-up coil gives rise to an output voltage as while the sample travels through it.

The SQUID composed mainly three important parts: (i) a superconducting magnet to generate externally applied field (*H*), (ii) sample transporting system to produce a response as shown in Fig. 2.5 (b), and (iii) pick up coil to read the response. The sample space is coupled with some form of temperature control systems such as cryogenic cooling or sample heating. The superconducting magnet can be charged with a current that gives rise to a static, homogeneous, (*dc*) field. When the sample moves up and down by a sample transporting system through the superconducting pick-up coil which actually has four windings, an alternating magnetic flux generates in the pick-up coil, leading to an alternating output voltage of the SQUID device. This voltage is then amplified and read out by the magnetometer's electronics. Temperature-dependent magnetization measurement (M vs. T) at the constant magnetic field (*H*); and measurements of magnetization vs. the applied field (M vs. H) can easily be evaluated using *a dc*-SQUID magnetometer. These

Figure 2.6. Photograph of the magnetic property measurement system (MPMS) based on a superconducting quantum interface device installed at Low-Temperature Center, Applied Physics and Quantum Computation Science department in Kyushu University that was used to measure the present studied compounds.

measurements can be used to determine the number of properties related to magnetic materials such as magnetic transition temperatures, saturation magnetization, Weiss temperature, etc.

In the current research, the SQUID facilities of Low-Temperature Center, Applied Physics and Quantum Computation Science Department in Kyushu University, as portrayed in Fig 2.6 was used to measure the magnetic measurement of the present studied compounds which could be able to measure low field like 5×10^{-18} T in the 2-300 K temperature range. The present studied samples were loaded into the gelatin capsule; after that, the capsule was inserted into a clear plastic straw, which was then mounted onto the brass sample rod. This configuration gives rise to the minimal background. The measurement was carried out at 2-300 K at H = 1.0 T along with Zero filled cool (ZFC) and Field cool (FC) conditions.

Chapter-3

Magnetism in Kagome Antiferromagnets $Mg_xMn_{4-x}(OH/D)_6Cl_2$

3.1. Synthesis and Characterization of $Mg_xMn_{4-x}(OH/D)_6Cl_2$ compounds

For nonmagnetic ion substitution into $Mn_4(OH)_6Cl_2$, the Mg ion is more effective than Zn ion, which may be accounted for by its smaller ion radius. The $MgCl_2.6H_2O$ and $MnCl_2.4H_2O$ compound were mixed in a beaker with a molar ratio of Mg/Mn = 0.5 to 3 in water-ethanol solution at the nitrogen atmosphere. The NaOH was added with this mixture dropwise to control the *p*H of the solution. After mixing NaOH, the final solution was transferred to the 50 ml Teflon lined stainless steel autoclave and tighten very carefully. The autoclave was then allowed to heat at 150-200°C temperature for 120 hours in a muffle furnace (DMT-01, SHIMPO, Japan), as shown in Fig. 3.1 (a). After the end of heating, the final product was washed with ethylene glycol at a nitrogen atmosphere to remove the unreacted $MgCl_2$ and NaCl content from the sample. The sample was dried at low pressure at around 100°C temperature in a vacuum (exposure to air or water containing oxygen would cause oxidation to change the powder to brownish color on the surface) at around 24 hours. Since site mixing seemed inevitable as well as known in herbertsmithite, $Mg_xMn_{4-x}(OH)_6Cl_2$ compounds with the different ration of Mg/Mn were prepared to judge the effect of non-magnetic defects on the magnetism of $MgMn_3(OH)_6Cl_2$. The final compound was a white polycrystalline compound, as depicted in Fig. 3.1 (b).

As the background signal of hydrogen samples is expected to be very high in the neutron powder diffraction experiment, the deuterated sample $MgMn_3(OD)_6Cl_2$ was synthesized from dried $MgCl_2$, $MnCl_2$, and NaOD in D_2O-ethanol in the similar way of $Mg_xMn_{4-x}(OH)_6Cl_2$ compound. Room temperature powder x-ray diffraction (XRD) measurement was performed using a x-ray diffractometer (Cu $K\alpha$) at Analytical Research Center for Experimental

(a) (b)

Figure 3.1. Photograph of (a) muffle furnace that was used to grow $Mg_xMn_{4-x}(OH)_6Cl_2$ compound, (b) polycrystalline powder of $Mg_xMn_{4-x}(OH)_6Cl_2$ compound.

Sciences in Saga University to investigate the crystal structure of the compounds. The observed x-ray diffraction (XRD) data was then analyzed using computer-aided program RIETAN-FP [101] based on the Rietveld refinement process.

The temperature-dependent DC susceptibility measurements were carried out using a commercial superconducting quantum interference device magnetometer (MPMS; Quantum Design) at H = 1.0 T field along with zero field cool (ZFC) and field cool (FC) condition at low-temperature Center, Department of Applied Quantum Physics, Kyushu University, Japan. A neutron powder-diffraction experiment was performed on $MgMn_3(OD)_6Cl_2$ using the super-high resolution powder diffractometer (Super-HRPD) in the time of flight (TOF) mode at J-PARC, Japan. The TOF neutron diffraction data was analyzed using the Rietveld analysis software for J-PARC [102]. The collected neutron data were refined using the FULLPROF-suite software based on Rietveld refinement [101], assisted by the representation analysis program SARAh [112].

3.2. Structural Characterization of $Mg_xMn_{4-x}(OH/D)_6Cl_2$ compounds

The crystal structural refinement of x-ray powder diffraction data was done by Rietan-FP program based on Rietveld analysis as exemplified in Fig. 3.2 showed that the kagome-lattice compounds $Mg_xMn_{4-x}(OH)_6Cl_2$ were successfully synthesized by selectively replacing the Mn^{2+} ions in the triangular-lattice planes of its parent compound $Mn_2(OH)_3Cl$. The parent compound $Mn_2(OH)_3Cl$ crystallizes in orthorhombic structure with lattice constant a = 6.49 Å, b = 7.11 Å, and c = 9.52Å in space group *Pnma*, No. 62 [67,114], whereas the $Mg_xMn_{4-x}(OH)_6Cl_2$ was found to crystallize in a rhombohedral structure with space group *R*-3*m* (No. 166). The structural data of one sample of $Mg_{1.55}Mn_{2.45}(OH)_6Cl_2$ are summarized in Table 3.1 and illustrated in Fig. 3.3.

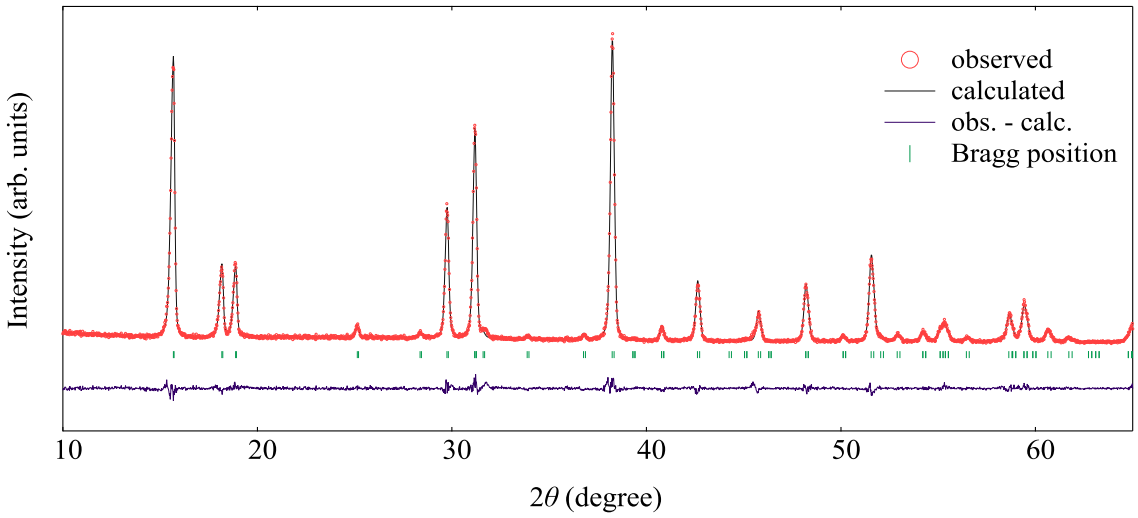

Figure 3.2: Powder x-ray diffraction pattern (red circles) for kagome lattice compound $Mg_{1.55}Mn_{2.45}(OH)_6Cl_2$ at room temperature and the result of Rietveld refinements showing the calculated (black solid line) pattern and the difference between the experimental and calculated data (thin violet solid line). The green bar represents the Bragg position of the present compound.

The triangular site (site 3*b* in the table) Mn ions were actually 98.0% replaced by Mg^{2+} ions; whereas 19.0% of the 9*e* kagome site Mn was also replaced. The 81% Mn^{2+} occupancy at the kagome site is higher than the percolation threshold for kagome ($p_c^{site} = 65\%$) [115]. As the non-magnetic defects may be an essential factor to influence the magnetism on the kagome lattice, we synthesized the compound using various conditions to produce various $Mg_xMn_{4-x}(OH)_6Cl_2$ around the nominal $MgMn_3(OH)_6Cl_2$, which all crystallized in an equivalent structure as summarized in Table 3.2 and compared x-ray diffraction (XRD) pattern are presented in Fig. 3.4. The Mg^{2+} ion prefers to occupy the octahedral triangular site of the present studied compound.

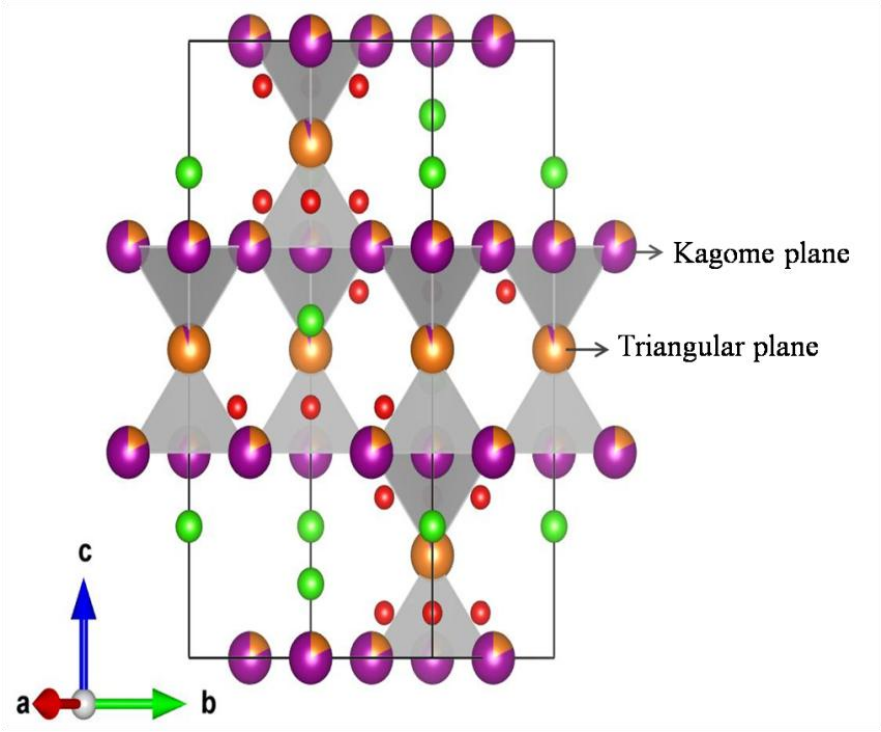

Figure 3.3: Crystal structure of $Mg_{1.55}Mn_{2.45}(OH)_6Cl_2$ showing alternately stacked layer of the kagome and triangular lattice planes along *c*-axis direction, where yellow, violet, green, and red colored sphere represents Mg^{2+}, Mn^{2+}, Cl^-, and O^{2-} ion, respectively.

Table 3.1. Crystal structural information of $Mg_{1.55}Mn_{2.45}(OH)_6Cl_2$ refined from x-ray diffraction at room temperature (site 9*e* and 3*b* correspond to kagome plane site and triangular site, respectively).

Chemical Formula			$Mg_{1.55}Mn_{2.45}(OH)_6Cl_2$				
Cell Setting			Rhombohedral				
Space group			*R*-3*m* (No.166)				
a (Å)			7.15420(4)				
c (Å)			14.80045(7)				
$\alpha = \beta = 90°, \gamma = 120°$							
R_{wp} (*S*)			9.6 (1.2)				
R_p			6.9				
	Site	Sym	*x*	*y*	*z*	*g*	*B*
Mg1	9*e*	.2/*m*	0.5	0	0	0.19(1)	1.125(8)
Mn1	9*e*	.2/*m*	0.5	0	0	0.81(1)	1.125(8)
Mg2	3*b*	-3*m*	0	0	0.5	0.98(1)	1.428(3)
Mn2	3*b*	-3*m*	0	0	0.5	0.02(1)	1.428(3)
Cl	6*c*	3*m*	0	0	0.2133(2)	1.0	1.975(2)
O	18*h*	.*m*	0.2015(3)	0.4030(6)	0.0730(2)	1.0	1.557(2)

For example, in the nominal formula of $Mg_{0.90}Mn_{3.10}(OH)_6Cl_2$, 66% of the triangular Mn were replaced by Mg, but only 8% of the kagome Mn were replaced. However, more Mg entered the kagome sites when Mn is heavily substituted. This situation is similar to that occurring in herbertsmithite $ZnCu_3(OH)_6Cl_2$, $(Mg/Zn)Co_3(OH)_6Cl_2$, and $MgFe_3(OH)_6Cl_2$. Although an ideal perfect kagome lattice cannot be realized, we can get a probable conclusion by investigating the magnetism evolution in the $Mg_xMn_{4-x}(OH)_6Cl_2$ samples with different degrees of substitution of the triangular lattice Mn and defects in the kagome lattice.

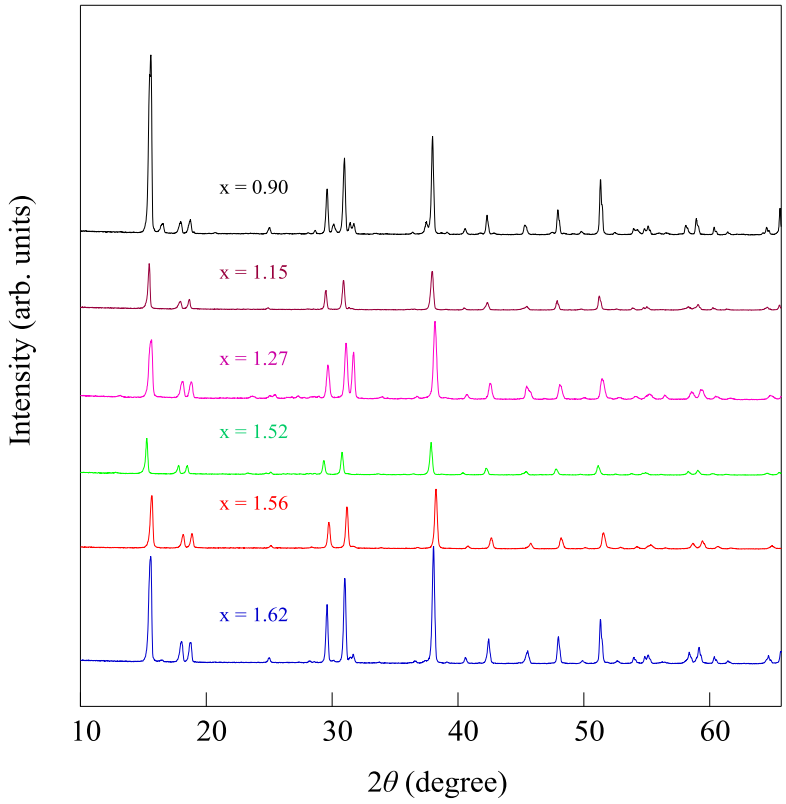

Figure 3.4. Powder X-ray diffraction data of kagome lattice compound $Mg_xMn_{4-x}(OH)_6Cl_2$ (x = 0.9 ~ 1.62).

Table 3.2. Summary of $Mg_xMn_{4-x}(OH)_6Cl_2$ compounds with varied total substitution rate *x*, substitution rate in kagome plane, and substitution rate in a triangular plane.

Compound formula	Total substitution rate *x*	Substitution rate in kagome plane	Substitution rate in triangular plane
$Mg_{0.90}Mn_{3.10}(OH)_6Cl_2$	0.90	0.08(1)	0.66(1)
$Mg_{1.15}Mn_{2.85}(OH)_6Cl_2$	1.15	0.10(2)	0.85(2)
$Mg_{1.27}Mn_{2.73}(OH)_6Cl_2$	1.27	0.11(2)	0.94(1)
$Mg_{1.50}Mn_{2.50}(OH)_6Cl_2$	1.50	0.18(2)	0.96(1)
$Mg_{1.55}Mn_{2.45}(OH)_6Cl_2$	1.55	0.19(1)	0.98(1)
$Mg_{1.62}Mn_{2.38}(OH)_6Cl_2$	1.62	0.21(3)	0.99(3)

The local environments of $Mg_{1.55}Mn_{2.45}(OH)_6Cl_2$ around the kagome, and triangular sites are illustrated in Fig. 3.5. The Mn/Mg (Mn1) at kagome site is surrounded by four O^{2-} and two Cl^- ions, whereas Mg/Mn (Mg2) in the triangular site is surrounded by six O^{2-} ions in the octahedral environment. Therefore, the selective replacement was enabled due to the different chemical environments for the Mn in the triangular lattice and kagome lattice planes. The bond lengths and bond angles around the Mn1, and Mn2 are listed in Table 3.3, which would help us to realize the superexchange mechanism in the present studied compound. The Mn1-O, and Mn1-Cl bond length around the kagome site are 2.174 Å and 2.724 Å, respectively; whereas the Mg-O bond length around the triangular site is 2.143 Å. In the kagome plane, each Mn^{2+} ion is bridged with another Mn^{2+} ion via O, or Cl ions, with angles of ∠Mn1-O-Mn1 = 110.7° and ∠Mn1-Cl-Mn1 = 82.1°. Analogous to the herbertsmithite $ZnCu_3(OH)_6Cl_2$, superexchange interactions should occur via the Mn1-O-Mn1 bridge, with possible additional coupling via Mn1-Cl-Mn1. The

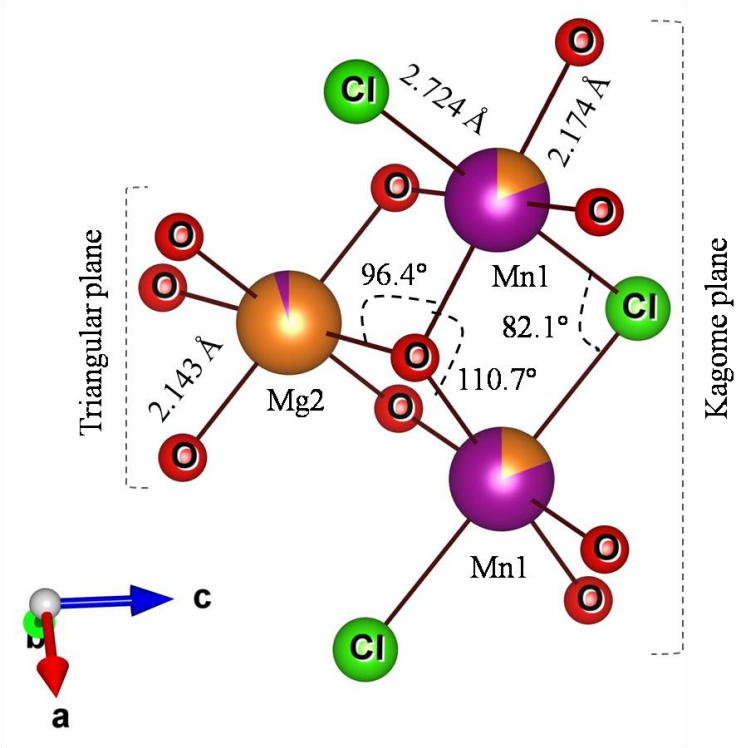

Figure 3.5. Local environment around the non-magnetic Mg^{2+} ion (yellow sphere) at the triangular site and the magnetic Mn^{2+} ion (violet sphere) at the kagome site.

Table 3.3. The bond lengths and bond angles around the Mn1, and Mn2 in the $Mg_{1.55}Mn_{2.45}(OH)_6Cl_2$ compound for an easy view of superexchange interaction.

Bond lengths (Å)			Bond angles (º)		
Mn1-O	:	2.174	∠Mn1-O-Mn1	:	110.7
Mn1-Cl	:	2.724	∠Mn1-Cl-Mn1	:	82.1
Mg-O	:	2.143	∠Mn1-O-Mn2	:	96.4

kagome Mn1 and residual triangular Mn2 is double bridged via two Mn1-O-Mn2 bonds angled ∠Mn1-O-Mn2 = 96.4°. These kinds of double bridges were seen in antiferromagnetic CuOHCl, as well as in $LiNiO_2$ and $NaNiO_2$ [116-119].

The refined lattice constants related to the substitution rate x in $Mg_xMn_{4-x}(OH)_6Cl_2$ for x = 0.9–1.62 are plotted in Fig.3.6. More specifically, those in relation to the substitution rates in the triangular plane x_{tri} and kagome plane x_{kag}, respectively, in $Mg_{xtri}Mn_{1-xtri}Mg_{3xkag}Mn_{3(1-xkag)}(OH)_6Cl_2$ are presented. The tendency of the variation of lattice constant is well seen in the x_{tri}. With substitution of Mn by smaller Mg, the c-axis length is slightly reduced till x_{tri} = 0.85. Meanwhile, the a-axis length, which depends on the ions in the kagome plane, remains almost unchanged. When x_{tri} exceeds 0.85, Mg also enters the kagome planes which will then effectively reducing the a-axis length. These consistent changes demonstrate the soundness of the structural analyses.

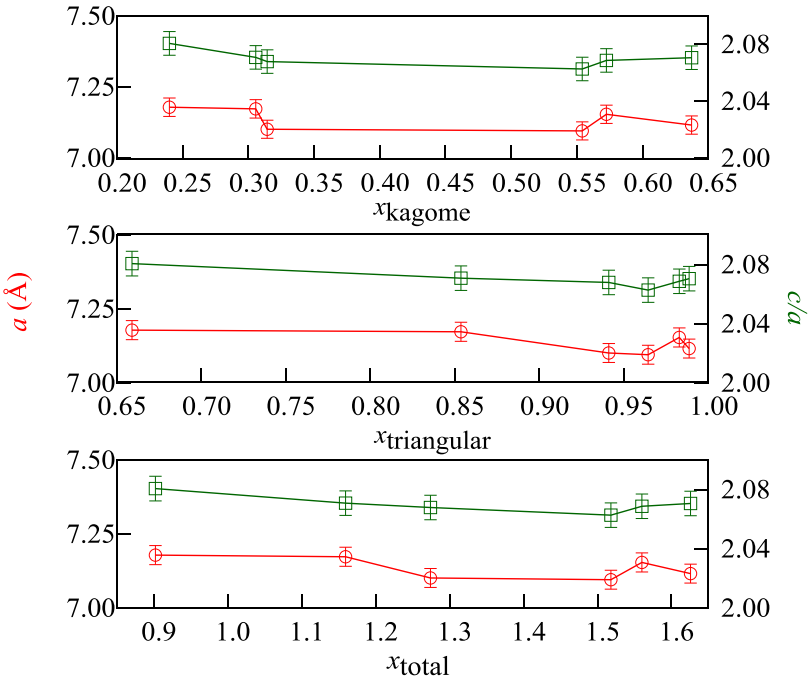

Figure 3.6. Variation of lattice constants related to Mg substitution ratios of the total substitution x, kagome plane substitution x_{kag}, and triangular plane substitution x_{tri} in $Mg_xMn_{4-x}(OH)_6Cl_2$.

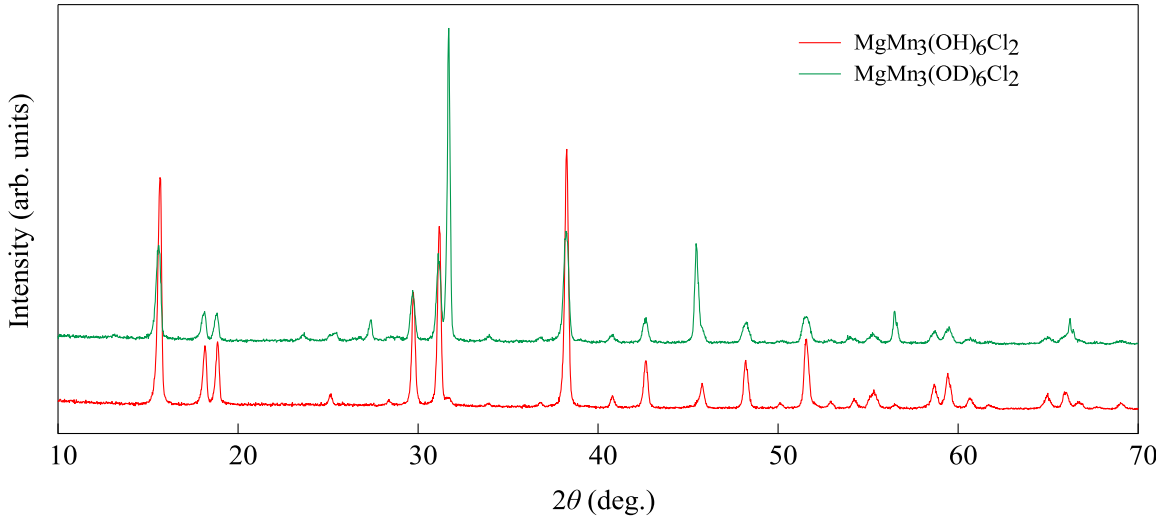

Figure 3.7. X-ray diffraction pattern of $MgMn_3(OD)_6Cl_2$ compared with the $MgMn_3(OH)_6Cl_2$ which depict almost similar patter except some impurity peaks.

The deuterated kagome lattice compound $MgMn_3(OD)_6Cl_2$ was synthesized to perform a neutron powder diffraction experiment. The x-ray diffraction data of $MgMn_3(OD)_6Cl_2$ has compared with that of $MgMn_3(OH)_6Cl_2$, which suggests that the $MgMn_3(OD)_6Cl_2$ compound has successfully crystallized in rhombohedral structure with R-3*m* space group except some of the non-magnetic peaks (NaCl peaks) in the x-ray pattern.

3.3. Temperature-dependent Magnetic Measurements of $Mg_xMn_{4-x}(OH)_6Cl_2$ Compound

The temperature dependence of dc susceptibility measurements taken at H = 1.0 T of all kagome lattice compounds, $Mg_xMn_{4-x}(OH)_6Cl_2$ (x = 0.9–1.62) showed similar magnetic behaviors with slightly different T_N values. The temperature dependence of dc susceptibility and inverse susceptibility of $Mg_{1.50}Mn_{2.50}(OH)_6Cl_2$ compound is shown in Fig. 3.8. This compound shows antiferromagnetic transition at T_N = 7.9 K, which was much enhanced than that of its parent compound $Mn_2(OH)_3Cl$ of T_{N1} = 3.4 K and T_{N2} = 2.7K [67]. All the kagome lattice compounds,

$Mg_xMn_{4-x}(OH)_6Cl_2$ (x = 0.9–1.62) showed a low-temperature upturn in their susceptibility measurement similar to that observed in $MgFe_3(OH)_6Cl_2$ [6], which is a common feature in geometrically frustrated systems reflecting spin fluctuations. The susceptibility curve also shows a small anomaly at ~40 K, which was suspected to be due to trace impurity of manganese oxides formed on the powder surface due to oxidation in air.

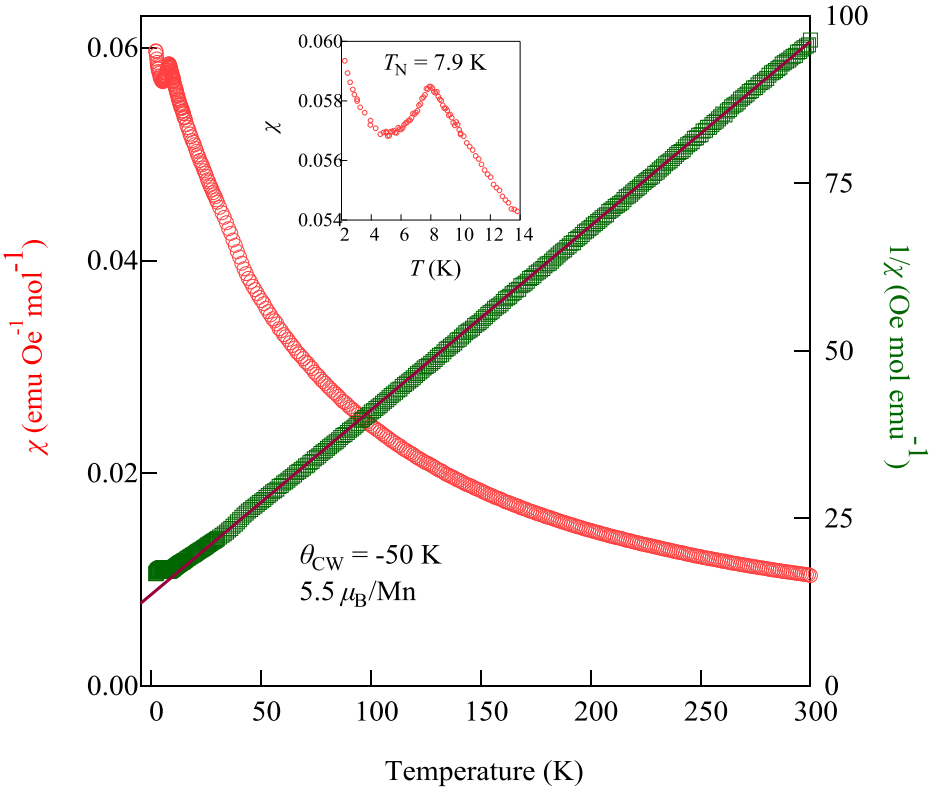

Figure 3.8. Temperature-dependence of dc susceptibilities χ (Left axis, open red circles), inverse susceptibilities $1/\chi$ (Right axis, open dark green squares) per mole Mn for $Mg_{1.50}Mn_{2.50}(OH)_6Cl_2$ measured at H = 10 kOe. The solid line obeys the Curie-Weiss law, with Weiss temperature of θ_{CW} of approximately -50 K. The inset plot is an enlarged view of temperature dependence susceptibilities (χ) plot up to 14 K showing the antiferromagnetic transition.

Moreover, susceptibility measurements at zero-field cooled (ZFC) and field-cooled (FC) conditions confirmed that it agreed well with the T_C = 40 K ferromagnetic Mn_3O_4 [120]. Though glassiness was found in the x = 0 compound $Mn_2(OH)_3Cl$, notable glassiness was not recognized in $Mg_xMn_{4-x}(OH)_6Cl_2$ for x = 0.9–1.62, except the ZFC/FC diverging starting from 40 K due to suspected partial oxidation to ferromagnetic Mn_3O_4.

The Curie-Weiss temperature (θ_{CW}) was calculated by fitting the temperature-dependent inverse susceptibility curve using the following relation [121]- $\chi^{-1}(T) = (T- \theta_{CW})/C$; where C is the Curie constant. The Curie-Weiss temperature was estimated to be θ_{CW} = −50 K, showing a much reduced geometrical frustration index of $f = \theta_{CW}/T_N \sim 6.3$, compared to the f = 17 in $Mn_2(OH)_3Cl$. A similar tendency of reduced frustration from the pyrochlore parent compounds to kagome compounds was seen in $MgFe_3(OH)_6Cl_2$ [6]. The estimated effective magnetic moment per Mn^{2+} ion to be 5.5 μ_B, which is slightly smaller than the spin only moment $\mu_{mag}^{calc.} = g\mu_B\sqrt{S(S+1)} = 5.92\,\mu_B$ for S = 5/2 Mn^{2+}. This value is close to the experimentally reported $\mu_{mag}^{obs.} = 5.6 - 6.1\mu_B$ for normal type Mn^{2+}, wherein the orbital contribution to the spin-only values for ions of the first transition period leads to somewhat smaller or larger effective magnetic moments.

The variation of transition temperature (T_N) with respect to the substitution of Mg in $Mg_xMn_{4-x}(OD)_6Cl_2$ (x= 0.90 – 1.62) is presented in Fig. 3.9, which reveals that the substitution range the T_N was enhanced by more completely replacing Mn in the triangular plane with Mg. It is evident that the transition temperature (T_N) slightly varied from 7.6–8.0 K, suggesting that the non-magnetic defects in the kagome site did not have a substantial effect on the ordering.

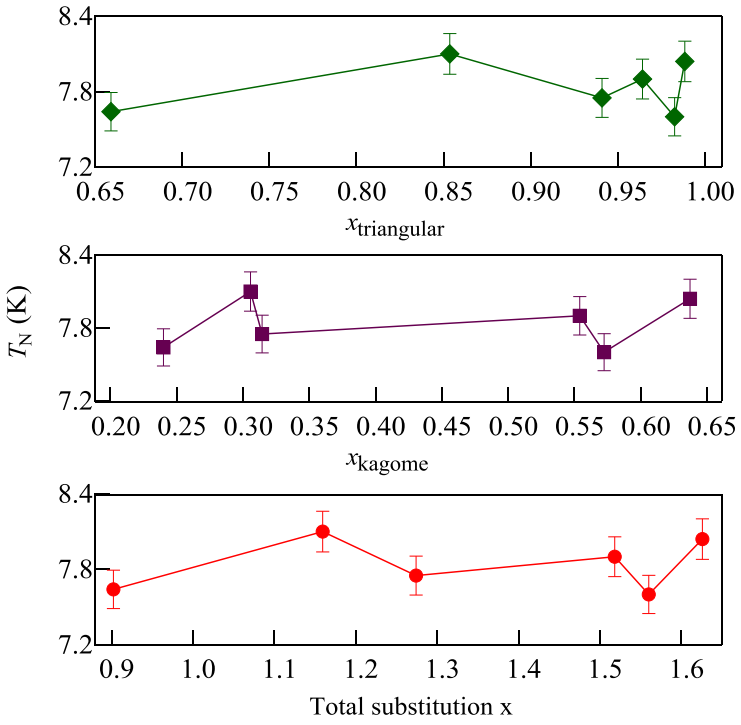

Figure. 3.9. Variation of transition temperature T_N related to Mg substitution ratio of the total substitution *x*, kagome plane substitution x_{kag}, and triangular plane substitution x_{tri} in $Mg_xMn_{4-x}(OD)_6Cl_2$ (x = 0.9 to 1.62).

3.4. Neutron powder diffraction measurements of $MgMn_3(OD)_6Cl_2$ Compounds

The neutron powder diffraction data measured at 20 K for $Mg_{1.34}Mn_{2.66}(OD)_6Cl_2$ and the results of Rietveld refinement are presented in Fig. 3.10 and Table 3.4 in which the atomic position of deuterium (D) was added as compared to Table 3.1 for $Mg_xMn_{4-x}(OH)_6Cl_2$. The $Mg_{1.34}Mn_{2.66}(OD)_6Cl_2$ compound crystallized in rhombohedral structure with space group R-3*m* analogous to $MgMn_3(OH)_6Cl_2$ in which Mn^{2+} ion stake alternatively on kagome lattice plane and triangular lattice plane, respectively, as depicted in Fig. 3.11.

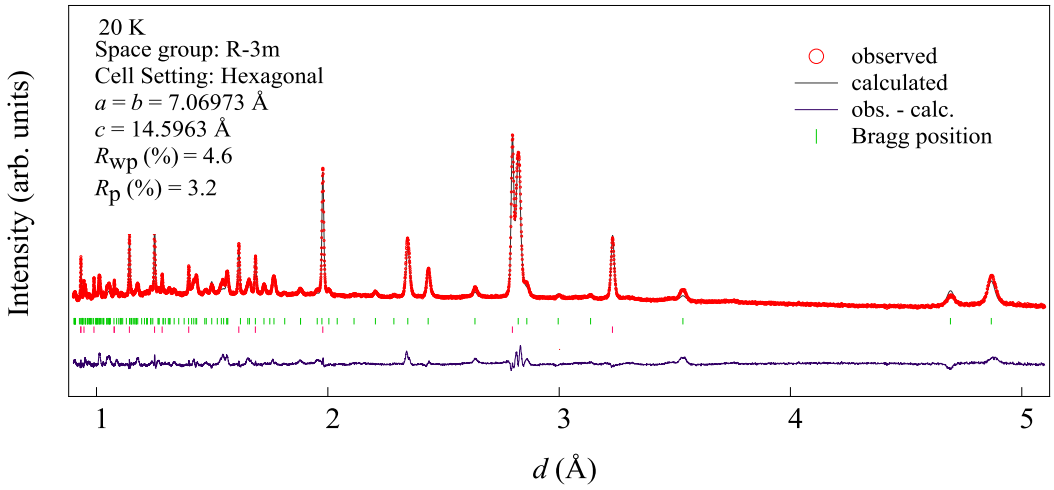

Figure 3.10. Neutron powder diffraction pattern (red circles) for $MgMn_3(OD)_6Cl_2$ at 20 K and the result of Rietveld refinements showing the calculated (solid black line) pattern and the difference between the experimental and calculated data (thin violet solid line). The vertical green bars represent the Bragg positions of the present compound. The specimen contained some accidentally included NaCl due to insufficient washing during preparation, as indicated by the violet bars under the Bragg positions of $MgMn_3(OD)_6Cl_2$.

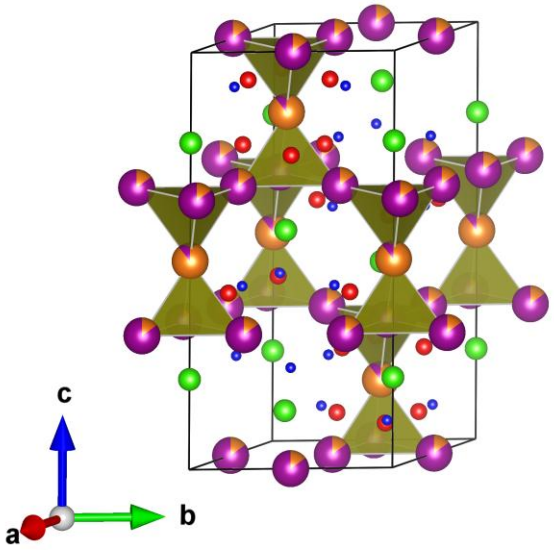

Figure 3.11: Crystal structure of $MgMn_3(OD)_6Cl_2$ in which Mn^{2+} ion stacks alternatively on the kagome-and triangular lattice planes, respectively. The blue sphere confirms the position of deuterium (D) in the compound.

Table 3.4. Crystal structural information of kagome lattice compound $Mg_{1.34}Mn_{2.66}(OD)_6Cl_2$ refined by Z-Rietveld based on Rietveld refinement of neutron powder diffraction at 20 K (site 9*e* and 3*b* correspond to the kagome plane site and triangular plane site, respectively).

Chemical Formula			$Mg_{1.34}Mn_{2.66}(OD)_6Cl_2$				
Cell Setting			Rhombohedral				
Space group			*R*-3*m* (No.166)				
a (Å)			7.06973(4)				
c (Å)			14.59632(2)				
$\alpha = \beta = 90°, \gamma = 120°$							
R_{wp} (%)			4.9				
R_p (%)			3.7				
	Site	Sym	*x*	*y*	*z*	*g*	*B*
Mg1	9*e*	.2/*m*	0.5	0	0	0.15(3)	0.6342(2)
Mn1	9*e*	.2/*m*	0.5	0	0	0.85(3)	0.6342(2)
Mg2	3*b*	-3*m*	0	0	0.5	0.89(7)	0.9592(7)
Mn2	3*b*	-3*m*	0	0	0.5	0.11(7)	0.9592(7)
Cl	6*c*	3*m*	0	0	0.2180(3)	1.0	1.1016(4)
O	18*h*	.*m*	0.2079(1)	0.4158(2)	0.0719(1)	1.0	1.2140(4)
D	18*h*	.*m*	0.1424(2)	0.2848(4)	0.0975(1)	1.0	1.1413(4)

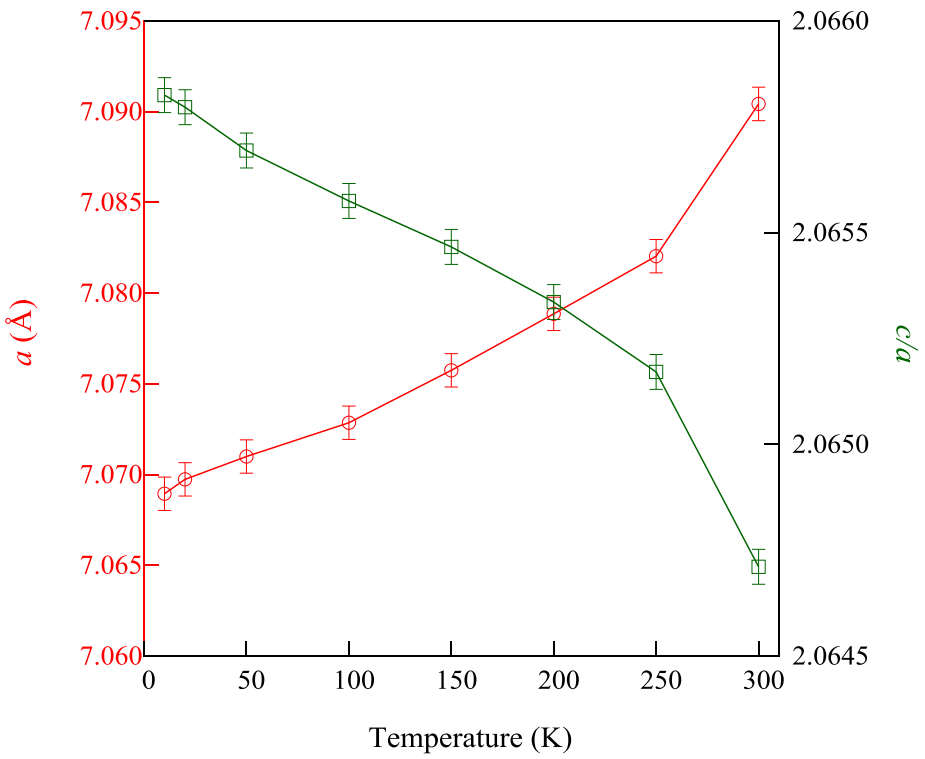

Figure 3.12. Temperature-dependence of lattice constant *a* (left axis, filled red circles) and the ratio of *c/a* for $MgMn_3(OD)_6Cl_2$ (right axis, filled green squares).

Neutron powder diffraction experiments were also performed at various temperatures to see the effect of change of temperature on the lattice constants. There was no structural transition occur except a prominent increase of the lattice constant ration c/a with decreasing temperature, as shown in Fig. 3.12.

Neutron powder diffraction pattern at 20 and 2.7 K, and their difference data are plotted in Fig. 3.13. Neutron data reveals that long-range antiferromagnetic order developed below 8 K in $Mg_{1.34}Mn_{2.66}(OD)_6Cl_2$ compound. The difference curve clearly demonstrates magnetic reflections appear at (0, 1, 1/2), (1, 0, 5/2), and (1, -1, 7/2) Bragg position with propagation vector $\boldsymbol{k}$ = (0, 0, 3/2). The critical exponent β was estimated to be β = 0.35(3) using the relation, $I = I_0(1 - T/T_N)^{2\beta}$ [122-123] by fitting the temperature dependence of integrated intensities of the (0, 1, 1/2) Bragg reflection, wherein T_N = 7.5(1) K.

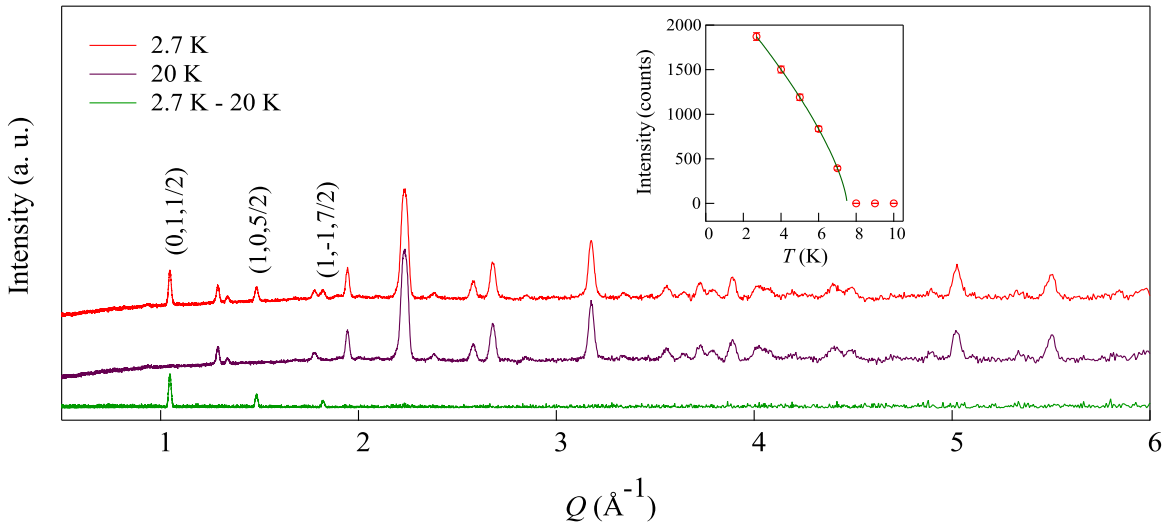

Figure 3.13. Neutron powder-diffraction patterns of $Mg_{1.34}Mn_{2.66}(OD)_6Cl_2$ at 2.7 and 20 K. The inset plot depicts the integrated intensity change of the (0, 1, 1/2) magnetic peak with respect to temperature for $Mg_{1.34}Mn_{2.66}(OD)_6Cl_2$. The solid line is the power-law fit $I = I_0(1 - T/T_N)^{2\beta}$.

This value is close to the β =0.355(17) in its sister compound S=2 Heisenberge spin $MgFe_3(OH)_6Cl_2$ [6] The theoretical critical exponents of several spin models are β = 0.253 for SO(2)xZ_2 in 3D, (n = 2), β = 0.125 for 2D Ising system, β = 0.365 for 3D Heisenberg spin system [124-127].

The SO(2)×Z_2 spin model corresponds to the frustrated XY triangular lattice antiferromagnet, whereas the rest of the spin models are non frustrated systems. The critical exponents usually depend on the symmetry of interaction, the dimensionally of the system, and the existence of frustration. By comparing the present experimental critical exponent to the theoretical values taking into consideration the factor of frustration, the present system can be viewed as a Heisenberg spin system. The result of the present spin system could be compared to the small β of 0.19(1) in the S = 5/2 kagome antiferromagnet $KFe_3(OH)_6(SO_4)_2$, wherein two-dimensional Ising symmetry due to the anisotropy was reported [128]. Therefore, unlike the present Heisenberg spin system of S = 5/2 $MgMn_3(OH)_6Cl_2$, the S = 5/2 jarosites should be rather viewed as an Ising system.

3.4. Proposed Magnetic Structure Calculation in Kagome Plane of $MgMn_3(OD)_6Cl_2$ compound by SARAh

Simulated annealing irreducible representation (SARAh) program [112] was used to derive all symmetric allowed magnetic structures. The possible magnetic structures for magnetic propagation vector $\boldsymbol{k}$ = (0, 0, 3/2) in the R-3*m* (No. 166) space group were found as- $\Gamma_{mag} = \Gamma_1(A_{1g})+2\Gamma_3(A_{2g})+6\Gamma_5(E_g)$, in which Γ_i indicates irreducible representations (IR). There is one basis vector for Γ_1, two basis vectors for Γ_3, and six basis vectors for Γ_5 in this structure.

Fifteen magnetic models with the combination of two basis vector given by ${}_6C_2=15$ were verified for Γ_5 irreducible representation giving a total of seventeen magnetic models, i.e., Γ_1 and Γ_2 each belong to one magnetic model and Γ_5 has fifteen magnetic models. The calculated magnetic moments of Mn^{2+} ion (Mn1) in kagome plane (i.e., at site Mn1_1, Mn1_2 Mn1_3) and fitting of observed neutron data with calculated data after Rietveld refinement are furnished in Table 3.5 and depicted in Fig. 3.14 (a-q).

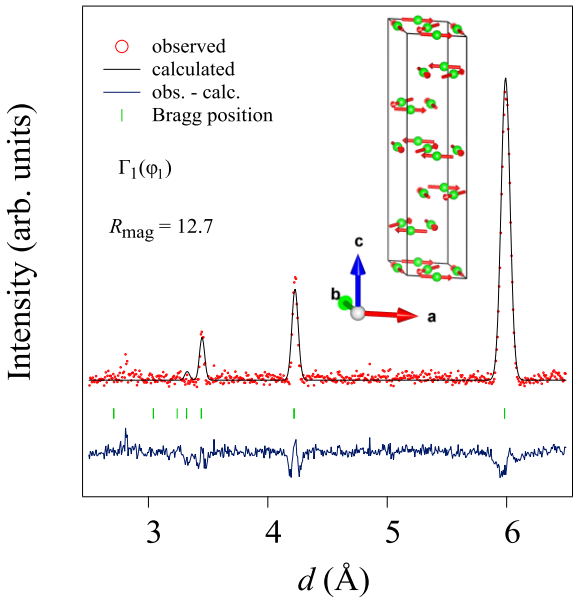

(a). $\Gamma_1(\varphi_1)$

Figure 3.14 (a). Rietveld refinement of difference data between 2.7 K and 20 K for $\Gamma_1(\varphi_1)$. The inset photograph shows the spin arrangement of Mn^{2+} ion in kagome plane.

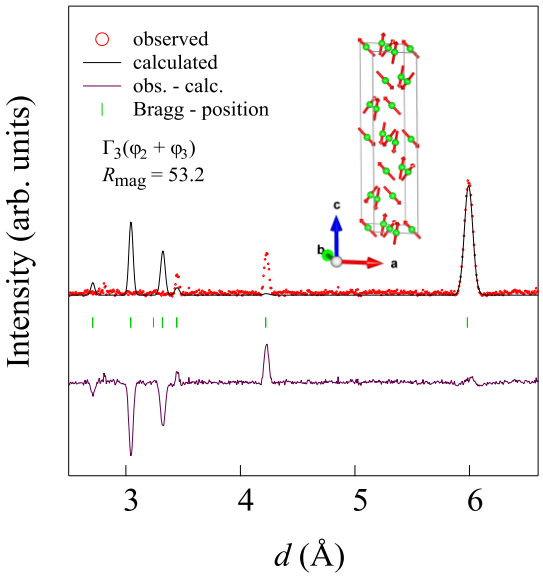

(b). $\Gamma_3(\varphi_2+\varphi_3)$

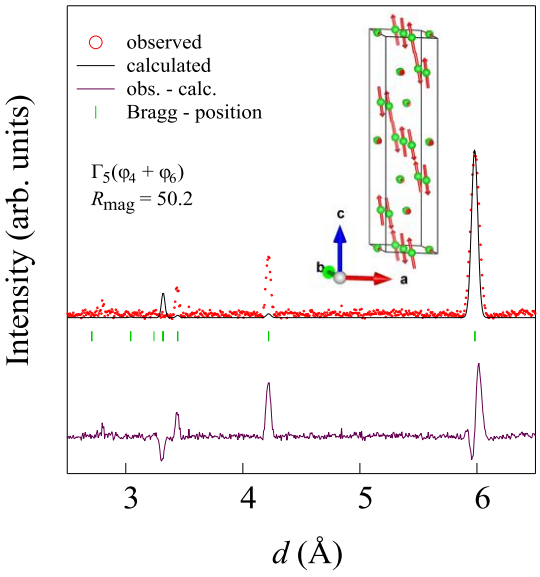

(d). $\Gamma_5(\varphi_4+\varphi_6)$

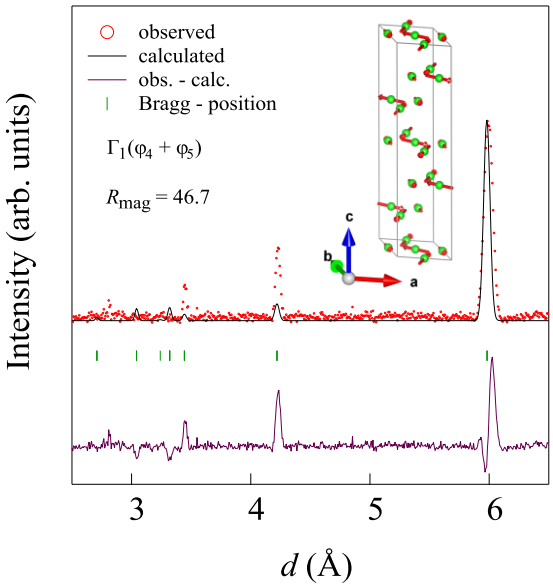

(c). $\Gamma_5(\varphi_4+\varphi_5)$

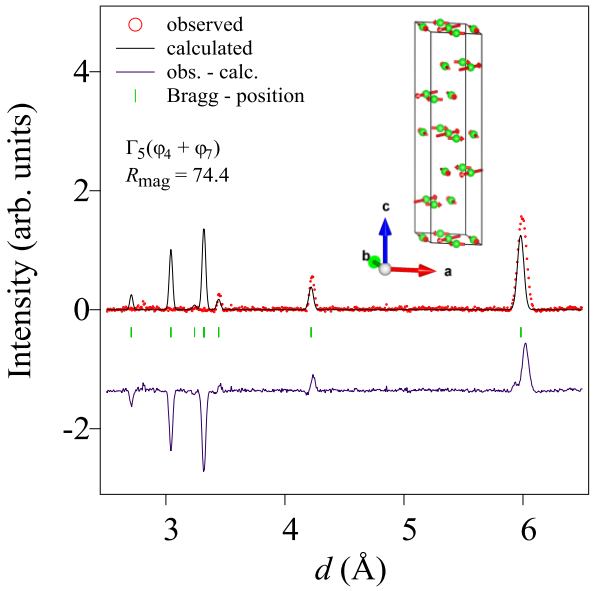

(e). $\Gamma_5(\varphi_4+\varphi_7)$

Figure 3.14 (b-e). Rietveld refinement of difference data between 2.7 K and 20 K for $\Gamma_3(\varphi_2+\varphi_3)$, $\Gamma_5(\varphi_4+\varphi_5)$, $\Gamma_5(\varphi_4+\varphi_6)$, and $\Gamma_5(\varphi_4+\varphi_7)$, respectively. The inset photograph shows the spin arrangement of Mn^{2+} ion in kagome plane.

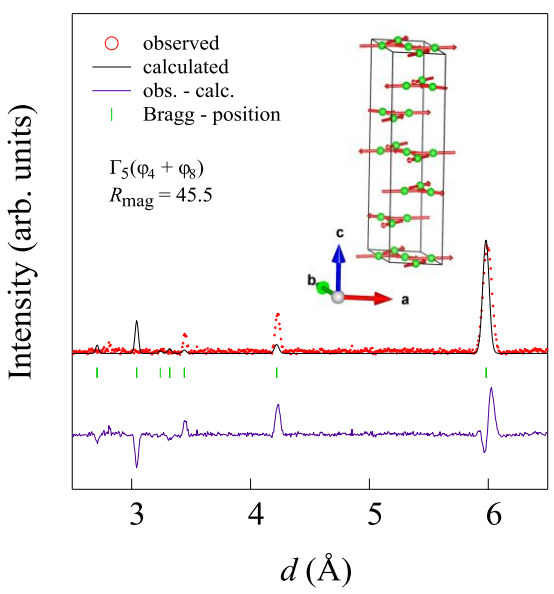

(f). $\Gamma_5(\varphi_4+\varphi_8)$

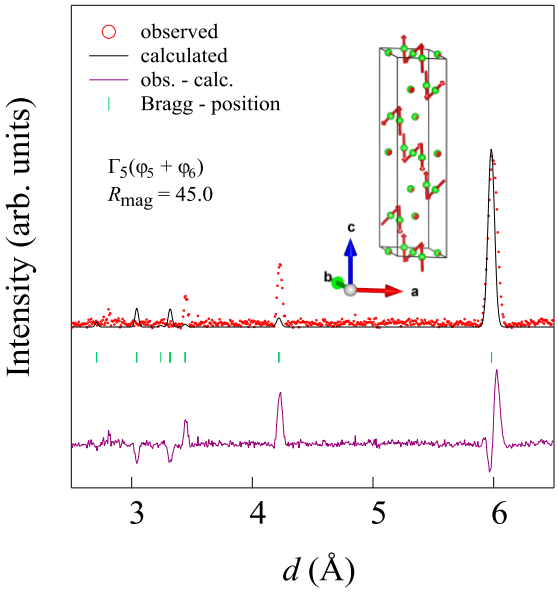

(h). $\Gamma_5(\varphi_5+\varphi_6)$

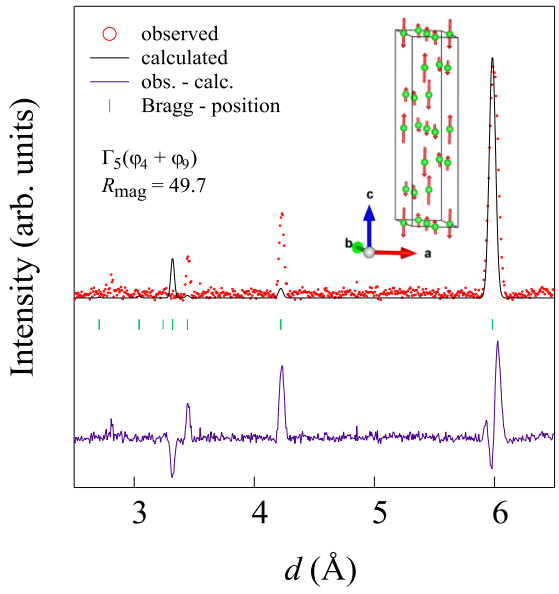

(g). $\Gamma_5(\varphi_4+\varphi_9)$

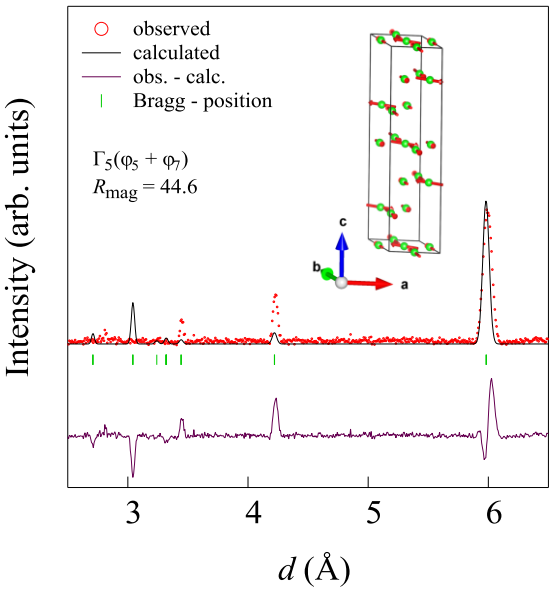

(i). $\Gamma_5(\varphi_5+\varphi_7)$

Figure 3.14 (f-i). Rietveld refinement of difference data between 2.7 K and 20 K for $\Gamma_5(\varphi_4+\varphi_8)$, $\Gamma_3(\varphi_4+\varphi_9)$, $\Gamma_5(\varphi_5+\varphi_6)$, $\Gamma_5(\varphi_5+\varphi_7)$, respectively. The inset photograph shows the spin arrangement of Mn^{2+} ion in kagome plane.

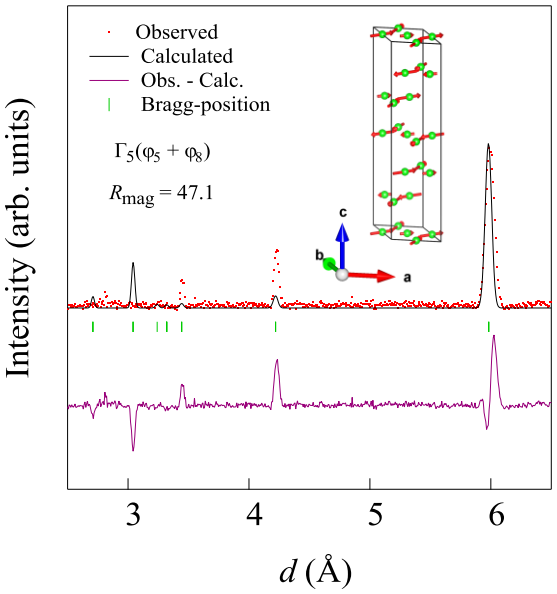

(j). $\Gamma_5(\varphi_5+\varphi_8)$

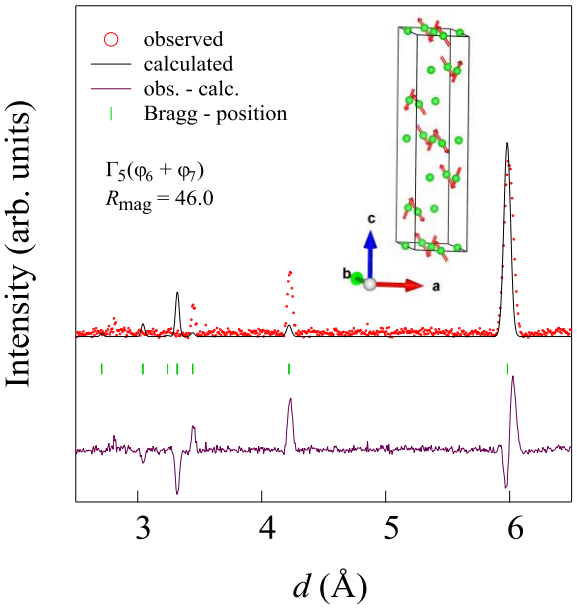

(l). $\Gamma_5(\varphi_6+\varphi_7)$

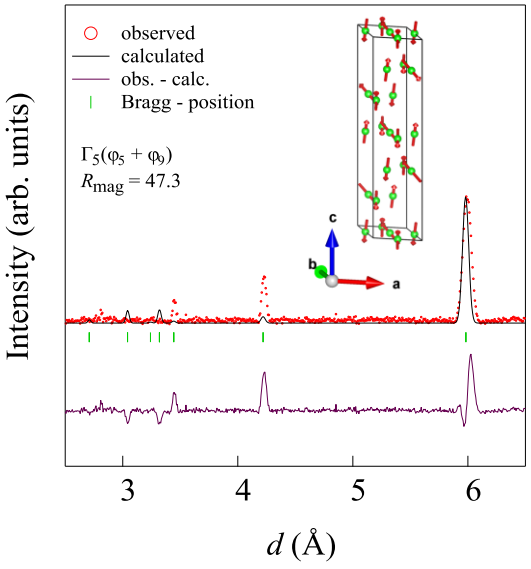

(k). $\Gamma_5(\varphi_5+\varphi_9)$

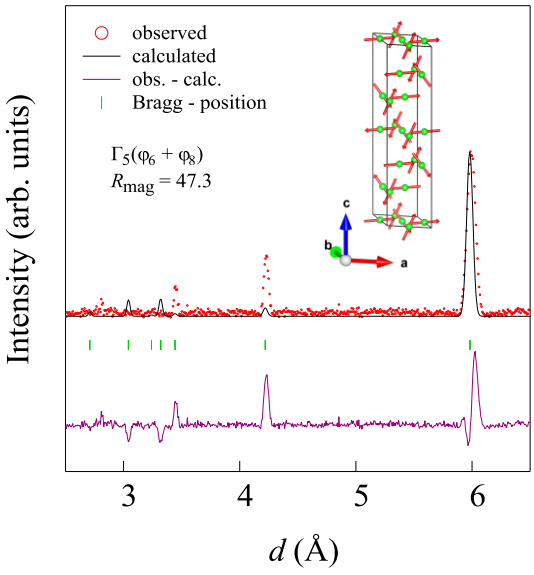

(m). $\Gamma_5(\varphi_6+\varphi_8)$

Figure 3.14 (j-m). Rietveld refinement of difference data between 2.7 K and 20 K for $\Gamma_5(\varphi_5+\varphi_8)$, $\Gamma_3(\varphi_5+\varphi_9)$, $\Gamma_5(\varphi_6+\varphi_7)$, $\Gamma_5(\varphi_6+\varphi_8)$, respectively. The inset photograph shows the spin arrangement of Mn^{2+} ion in kagome plane.

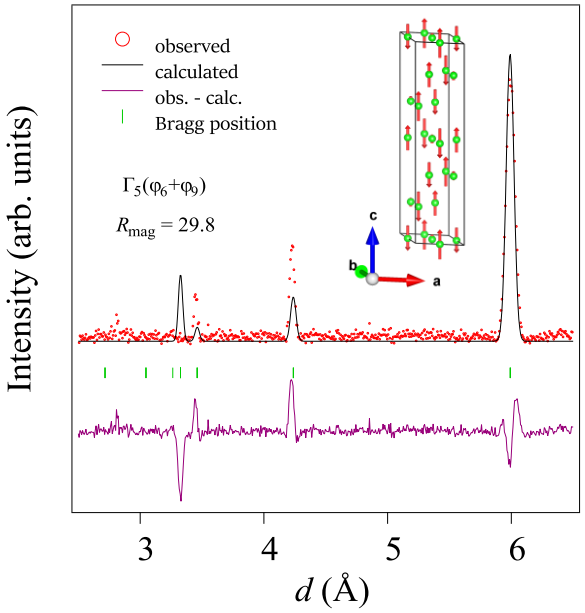

(n). $\Gamma_5(\varphi_6+\varphi_9)$

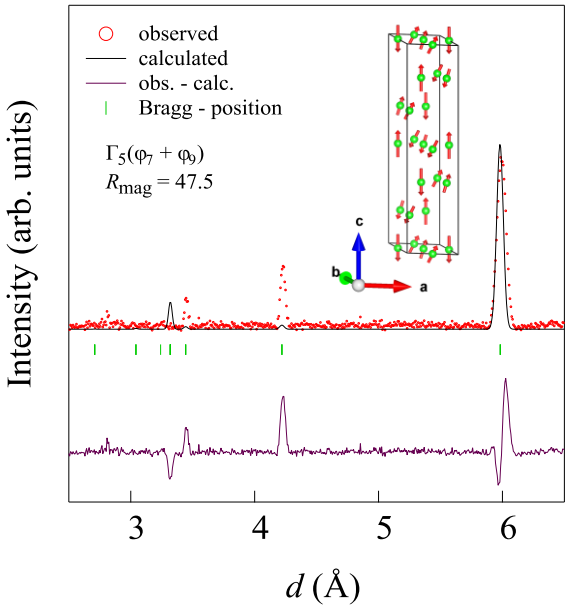

(p). $\Gamma_5(\varphi_7+\varphi_9)$

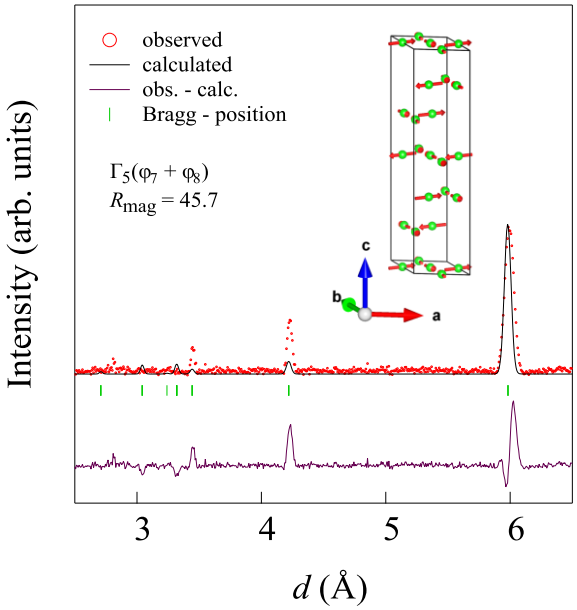

(o). $\Gamma_5(\varphi_7+\varphi_8)$

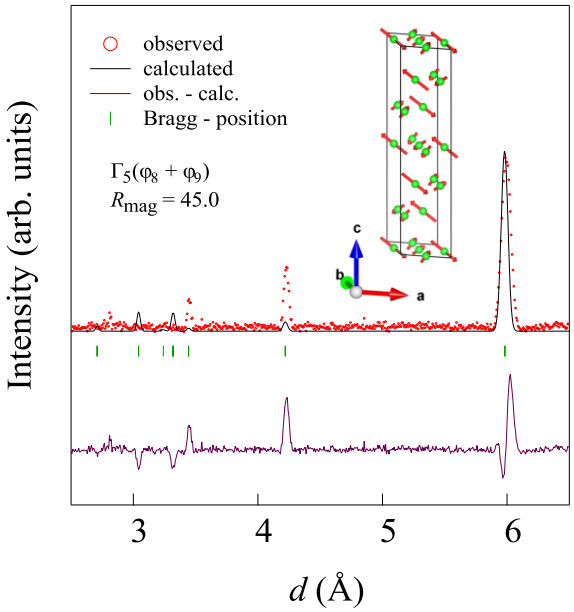

(q) $\Gamma_5(\varphi_8+\varphi_9)$

Figure 3.14 (n-q). Rietveld refinement of difference data between 2.7 K and 20 K for $\Gamma_5(\varphi_6+\varphi_9)$, $\Gamma_3(\varphi_7+\varphi_8)$, $\Gamma_5(\varphi_7+\varphi_9)$, and $\Gamma_5(\varphi_8+\varphi_9)$, respectively. The inset photograph shows the spin arrangement of Mn^{2+} ion in kagome plane.

Table 3.5. Summary of magnetic moments of Mn^{2+} in kagome plane at three different sites, namely Mn1_1, Mn1_2, and Mn1_3 and magnetic reliable R-factor (R_{mag}) for all calculated magnetic structure of $MgMn_3(OD)_6Cl_2$ compound.

Calculated Magnetic Model	Magnetic moment (μ_B) of Mn^{2+} ion at three different positions in kagome plane			R_{mag}
	Mn1_1	Mn1_2	Mn1-3	
$\Gamma_1(\varphi_1)$	4.735	4.735	4.735	12.7
$\Gamma_3(\varphi_2+\varphi_3)$	4.488	4.488	4.488	53.2
$\Gamma_5(\varphi_4+\varphi_5)$	4.492	1.237	4.492	46.7
$\Gamma_5(\varphi_4+\varphi_6)$	2.444	0.879	2.444	50.2
$\Gamma_5(\varphi_4+\varphi_7)$	1.088	1.498	2.587	74.4
$\Gamma_5(\varphi_4+\varphi_8)$	0.948	1.499	0.758	45.4
$\Gamma_5(\varphi_4+\varphi_9)$	1.930	3.860	1.930	49.7
$\Gamma_5(\varphi_5+\varphi_6)$	3.235	0.934	3.235	45.0
$\Gamma_5(\varphi_5+\varphi_7)$	1.364	0.476	1.241	44.6
$\Gamma_5(\varphi_5+\varphi_8)$	4.023	5.087	2.106	47.1
$\Gamma_5(\varphi_5+\varphi_9)$	3.805	3.632	3.805	47.3
$\Gamma_5(\varphi_6+\varphi_7)$	5.987	0.0	5.987	46.0
$\Gamma_5(\varphi_6+\varphi_8)$	3.690	3.860	3.690	47.3
$\Gamma_5(\varphi_6+\varphi_9)$	4.492	3.611	0.881	29.8
$\Gamma_5(\varphi_7+\varphi_8)$	2.642	4.880	2.642	45.7
$\Gamma_5(\varphi_7+\varphi_9)$	1.554	2.769	1.554	47.5
$\Gamma_5(\varphi_8+\varphi_9)$	1.903	3.486	1.903	45.0

The best results of each irreducible representations (Γ_i) are compared in Fig 3.15. Out of 15 magnetic models for Γ_5, only $\Gamma_5(\varphi_6+\varphi_9)$ has the lowest magnetic reliable factor of R_{mag} = 29.8, as shown in Table 3.5. However, as shown in Fig. 3.15 the fitting is inconsistent to the experimental data, and it unreasonably produced different magnetic moments of 4.5, 3.6, and 0.88 μ_B for three crystallographically equivalent Mn ions in the kagome plane. The $\Gamma_3(\varphi_2+\varphi_3)$ produced a very poor fitting (R_{mag} = 53.2) with equivalent magnetic moments of 4.5 μ_B for the three Mn ions. The previously reported chirality −1 structures, as described for $MgFe_3(OD)_6Cl_2$ [6] gave even poorer fitting. The best-fitting was obtained with the irreducible representation $\Gamma_1(\varphi_1)$ with a small R_{mag} = 12.7 and an equivalent 4.7μ_B for the three Mn ions in the kagome lattice plane.

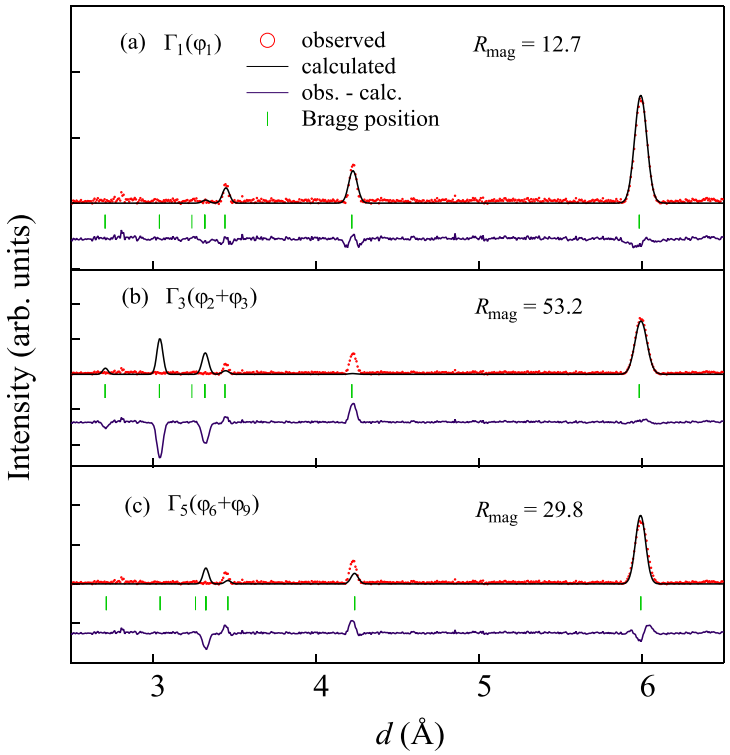

Figure 3.15. Observed magnetic reflections (red circles), calculated intensities (black solid line), and the difference between the experimental and calculated data (blue solid line) for: (a) $\Gamma_1(\varphi_1)$, (b) $\Gamma_3(\varphi_2+\varphi_3)$, and (c) $\Gamma_3(\varphi_6+\varphi_9)$ in $Mg_{1.34}Mn_{2.66}(OD)_6Cl_2$. The green bars represent the magnetic Bragg-peak positions.

Apparently, the $\Gamma_1(\varphi_1)$ with a 120° nearest-neighbor spin ordering confined on the kagome lattice plane, as visualized in Fig. 3.16 should represent the spin structure in $Mg_{1.34}Mn_{2.66}(OD)_6Cl_2$.

The direction of the spin vector in the individual triangles is related to the chirality of the spin, which is a necessary parameter in the kagome lattice antiferromagnets. The chirality vector is roughly defined by the relation [125] $\boldsymbol{K} = \left(\frac{2}{3\sqrt{3}}\right)[(\boldsymbol{S}_1 \times \boldsymbol{S}_2) + (\boldsymbol{S}_2 \times \boldsymbol{S}_3) + (\boldsymbol{S}_3 \times \boldsymbol{S}_1)$; where $\mathbf{S}_1$, $\mathbf{S}_2$, and $\mathbf{S}_3$ are the spins of the corner of the elemental triangle. The chirality is +1 or -1 when the spin rotates clockwise or counter clockwise by 120° step. The spin arrangement of $\Gamma_1(\varphi_1)$ has a spin chirality of $+1$ (clockwise). Since $\Gamma_1(\varphi 1)$ structure shows improved fitting along with good magnetic moment 4.7 μ_B for Mn^{2+} ion, therefore it can be concluded that the possible magnetic structure of the present studied compound composed with +1 spin-vector chirality by 120° spin steps.

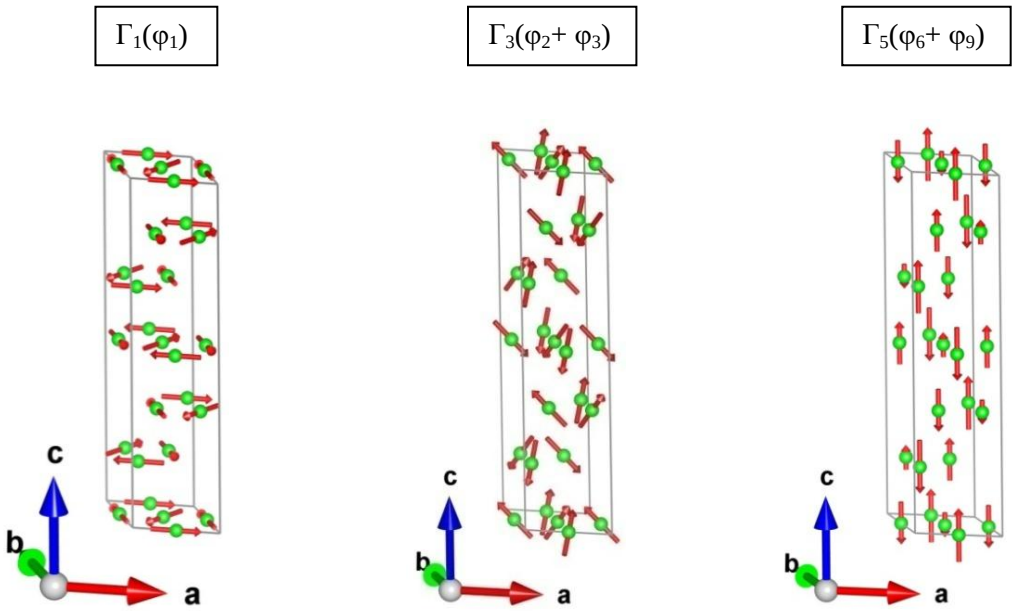

Figure 3.16. Illustration of the magnetic structures of $\Gamma_1(\varphi_1)$, $\Gamma_3(\varphi_2+\varphi_3)$, and $\Gamma_3(\varphi_6+\varphi_9)$ along *c* - direction derived for $MgMn_3(OD)_6Cl_2$.

3.6. General Discussions

The 120° spin ordering at a relatively high T_N = 8 K in $Mg_{1.34}Mn_{2.66}(OD)_6Cl_2$ is similar to that in its sister compound S =2 $MgFe_3(OD)_6Cl_2$ at T_N = 9.9K, though the latter has an opposite spin vector chirality −1. The long-range ordering exhibit in the present spin system at such high transition temperatures distinctly differ from those predicted for classical Heisenberg models by most theoretical investigations. Although Mg and Mn intermixing exists in the present $Mg_xMn_{4-x}(OH)_6Cl_2$ system, we tend to conclude that long-range ordering is intrinsic for the nominal $MgMn_3(OH)_6Cl_2$ for reasons described below.

First, all kagome antiferromagnets $Mg_xMn_{4-x}(OH)_6Cl_2$ (x = 0.9–1.62) crystallized with different Mg/Mn site intermixing showed similar magnetism, which suggests that the defects did not affect the ordering in $MgMn_3(OH)_6Cl_2$.

Second, the ordering in the present Heisenberg spin system $Mg_xMn_{4-x}(OH)_6Cl_2$ is strikingly different from the S = 3⁄2 Ising kagome antiferromagnets $ZnCo_3(OH)_6Cl_2$ and $MgCo_3(OH)_6Cl_2$, which have similar intermixing patterns but show partial spin liquid magnetism [76-77]. All of these results are consistent and support the intrinsic nature of the magnetic ordering in $MgMn_3(OH)_6Cl_2$ compound.

For a classical Heisenberg kagome antiferromagnet, most theoretical works predict a large ground state degeneracy or particular spin arrangements near T = 0. The Dzyaloshinskii-Moriya (DM) interaction may lead to ordering with the q = 0 phase with the all-in all-out structure [81], which was previously proposed to account for the unexpected LRO in jarosites. Both planar and weak ferromagnetic (along the axis perpendicular to the kagome plane) structures are obtained theoretically, which indeed agree with the experimentally observed results in jarosites. However, the Mn spin anisotropy in the present system appeared small. In addition, the magnetization of the samples did not show a DM-type weak-ferromagnetic property for $T < T_N$. Therefore, that kind of DM effect is considered to be absent. The high value of T_N = 8 K might be appears from order from disorder theories [50, 83-84]. Besides, these models predicted tripled-unit-cell spin structures, which are different from that in $Mg_xMn_{4-x}(OH)_6Cl_2$.

The present regular kagome lattice system could be compared to the so-called kagome–triangular (KT) lattice of layered fluoride $NaBa_2Mn_3F_{11}$ [129]. In the latter, a kagome type array of regular triangles composed of Mn^{2+} ions (spin 5/2) deforms much so as to generate a large next-nearest neighbor interaction J_2 in addition to the nearest-neighbor interaction J_1. This kagome-triangular (KT) lattice compound showed a long-range order (LRO) at 2.0 K, which is shown to be in good consistency with the unique noncoplanar magnetic orders predicted by the extended $J_1 - J_2$ model [87]. Indeed, the critical role of the next-nearest-neighbor interaction in inducing magnetic order in this kind of KT lattices has also been demonstrated in a triangular spin tube material $CsCrF_4$, wherein ferromagnetic kagome bond, single-ion anisotropy, and DM interaction play key roles in the selection of the ground state [130].

The present spin system could also be compared with the dipolar+Heisenberg interaction model as proposed by Maksymenko et al. [84] that predicted three-sublattice long-range order with coplanar 120° spin structure. The main exchange interaction *Je* can be estimated approximately to be J_e = −2.14 K from the Curie-Weiss temperature θ_{CW} using the mean-field theory by $J_e = \frac{3k_B\theta_{cw}}{2zJ(J+1)}$, where z is the number of nearest neighbors. The dipolar interaction energy D is estimated to be 0.46 K for the Mn^{2+} spin using the relation, $D = \frac{\mu_0}{4\pi}\frac{\mu^2}{R_{nm}^3}$, where R_{nm} = 0.358 nm. The long-range order in the present $Mg_xMn_{4-x}(OH)_6Cl_2$ compounds with D/Je = ~ 0.21 may be qualitatively explained by the dipolar+Heisenberg interactions model. However, the high T_N near 8 K seems not to be readily explainable. Most probably, dipolar+multiple Heisenberg interactions, including some inter kagome-plane couplings, would better describe the magnetic order in $MgMn_3(OH)_6Cl_2$. Especially, both $MgFe_3(OH)_6Cl_2$ of spin chirality−1 and $MgMn_3(OH)_6Cl_2$ of spin chirality +1 has an ordering wave vector $\boldsymbol{k}$ = (0, 0, 3/2), suggesting weak interplane superexchange interactions.

Chapter-4

Conclusions

In order to explore the ground state of the classical spin kagome antiferromagnet, the S = 5/2 classical kagome antiferromagnet $MgMn_3(OH)_6Cl_2$ has successfully synthesized using solvothermal reaction process. This kagome lattice compound crystallizes in rhombohedral structure with space group *R*-3m, in a similar crystal structure to the much researched quantum spin liquid candidate herbertsmithite $ZnCu_3(OH)_6Cl_2$. The substitution of non-magnetic Mg^{2+} ion into the parent compound of deformed pyrochlore $Mn_2(OH)_3Cl$ results 2D kagome lattice geometry, which displayed increased transition temperature T_N = 8.0 K with respect to $Mn_2(OH)_3Cl$ whose transition temperature at T_{N1} = 3.4 K and T_{N2} = 2.7 K. The increment of transition in the present spin system significantly reduce magnetic frustration with respect to its parent compound of deformed pyrochlore $Mn_2(OH)_3Cl$. Moreover, all the compounds present in $Mg_xMn_{4-x}(OH)_6Cl_2$ (x = 0.9 - 1.62) displayed transition temperature between 7.6 - 8.0 K despite different Mg/Mn sites intermixing, suggesting that the defects did not affect the magnetic ordering in the present system. A long-range coplanar magnetic order developed below approximately 8 K in $Mg_{1.34}Mn_{2.66}(OD)_6Cl_2$ as revealed by neutron powder diffraction experiment. This clearly shows that the magnetic ordering in the classical spin kagome $Mg_{1.34}Mn_{2.66}(OD)_6Cl_2$ is strikingly different from its Cu variant of the quantum Heisenberg antiferromagnet $ZnCu_3(OH)_6Cl_2$ in the same material series of magnetic transition metal hydroxyhalogenide. The experimentally obtained critical exponent β = 0.35 agrees with the three-dimensional Heisenberg spin system with a 120º nearest-neighbor spin structure confined in the kagome plane and spin-vector chirality of q = +1 below transition temperature (T_N). Recently, J. Merino et al. [78] reported theoretically rapid diminishing of quantum fluctuation with increasing the spin moment for honeycomb lattice. Our experimental verification of the magnetic ordering of S = 5/2 Heisenberg spin on a regular kagome lattice, and the previously reported S = 2 Heisenberg kagome antiferromagnet $MgFe_3(OH)_6Cl_2$, provides simple real systems for further theoretical and experimental studies on classical kagome antiferromagnets.

References

[1] Frustrated Spin System, edited by H. T. Diep (World Scientific, Singapore, 2013.

[2] Y. Zhou, K. Kanoda, and T.- K. Ng, Quantum spin liquid states, Rev. Mod. Phys. 89, 025003 (2017).

[3] M. J. P. Gingras, C. V. Stager, N. P. Raju, B. D. Gaulin, and J. E. Greedan, Static Critical Behavior of the Spin-Freezing Transition in the Geometrically Frustrated Pyrochlore Antiferromagnet $Y_2Mo_2O_7$, Phys. Rev. Lett. 78, 947 (1997).

[4] P. Mendels, F. Bert, M. A. de Vries, A. Olariu, A. Harrison, F. Duc, J. C. Trombe, J. S. Lord, A. Amato, and C. Baines, Quantum Magnetism in the Paratacamite Family: Towards an Ideal Kagomé Lattice, Phys. Rev. Lett. 98, 077204 (2007).

[5] P. Mendels and F. Bert, Quantum Kagome Frustrated Antiferromagnets: One Route to Quantum Spin liquids, Comp. Rend. Phys. 17, 455 (2016).

[6] M. Fujihala, X. G. Zheng, S. Lee, T. Kamiyama, A. Matsuo, K. Kindo, and T. Kawae, Spin Order in the Heisenberg Kagome Antiferromagnet $MgFe_3(OH)_6Cl_2$, Phys. Rev. B 96, 144111 (2017).

[7] A. S. Wills, and A. Harrison, R. Smith Magnetic Properties of Pure and Diamagnetically Doped Jarosites: Model Kagome Antiferromagnets with Variable Coverage of the Magnetic Lattice, Phys. Rev. B 61, 6156 (2000).

[8] A. P. Ramirez, Geometrical Frustration in Magnetism, Proceedings of the 21st International Conference on Low Temperature Physics, Prague, August 8-14, 1996, Czechoslovak Journal of Physics, Vol. 46, 91996).

[9] M. J. Harris and M. P. Zinkin, Modern Physics Letters B, 10, 417438 (1996).

[10] S. D. Barrett, The Structure of Rare-Earth Metal Surface (World Scientific).

[11] A. G. Maestro and M. J. Gingras, Quantum Spin Fluctuations in the Dipolar Heisenberg-Like Rare Earth Pyrochlores, J. of Phys.: Cond. Mat. 16, 3339 (2004).

[12] C. Lacroix, P. Mendels, and F. Mila, Introduction to Frustrated Magnetism (Springer

Series in Solid Sciences, 2011).

[13] N. N. Melnik, L. M. Tsapenko, V. I. Larchev, and G. G. Skrotskaya, Inorganic Materials, 26, 676 (1990).

[14] J. D. M. Champion, M. J. Harris, P. C. W. Holdsworth, A. S. Wills, G. Balakrishnan, S. T. Bramwell, T. Fennell, J. S. Gardner, J. Lago, D. F. McMorrow, M. Orendac, A. Orendacova, D. McK. Paul, R. I. Smith, M. T. F. Telling, and A. Wildes, Evidence of quantum order by disorder in a frustrated antiferromagnet, Physical Review B 68, 020401(2003).

[15] J. S. Gardner, S. R. Dunsiger, B. D. Gaulin, M. J. P. Gingras, J. E. Greedan, R. F. Kiefl, M. D. Lumsden, W. A. MacFarlane, N. P. Raju, J. E. Sonier, I. Swainson, and Z. Tun, Cooperative Paramagnetism in the Geometrically Frustrated Pyrochlore Antiferromagnet $Tb_2Ti_2O_7$, Phys. Rev. Lett. 82, 1012 (1999).

[16] H. Takatsu, H. Kadowaki, T. J. Sato, J. W. Lynn, Y. Tabata, T. Yamazaki, and K. Matsuhira, Quantum Spin Fluctuations in the Spin-Liquid State of $Tb_2Ti_2O_7$, J. Phys: Cond.. Matt., 24, 052201 (2011).

[17] M. J. P. Gingras, B. C. den Hertog, M. Faucher, J. S. Gardner, S. R. Dunsiger, L. J. Chang, B. D. Gaulin, N. P. Raju, and J. E. Greedan, Thermodynamic and Single-ion Properties of Tb^{3+} within the Collective Paramagnetic-spin Liquid State of the Frustrated Pyrochlore Antiferromagnet $Tb_2Ti_2O_7$, Phys. Rev. B 62, 6496 (2000).

[18] M. A. Subramanian, G. Aravamudan, G. V. Subba Rao, Oxide Pyrochlores - A review, Prog. in Solid State Chem. 15, 55 (1983).

[19] S. Miyashita, and Hiroyuki, Nature of the Phase Transition of the Two-Dimensional Antiferromagnetic Plane Rotator Model on the Triangular Lattice, J. Phys. Soc. Japan 53, 1145 (1983).

[20] S. Miyashita, and H. Kawamura, Phase Transition of the Heisenberg Antiferromagnet on the Triangular Lattice in a Magnetic Field, J. Phys. Soc. Japan 54, 3385 (1985).

[21] S. Miyashita, Magnetic Properties of Ising-Like Heisenberg Antiferromagnets on the

Triangular Lattice, J. Phys. Soc. Japan 55, 3605 (1986).

[22] S. Yamashita, Y. Nakazawa, M. Oguni, Y. Oshima, H. Nojiri, Y. Shimizu, K. Miyagawa, K. Kanoda, Thermodynamic Properties of a Spin-1/2 Spin-Liquid State in a k-type Organic Salt. Nat. Phys. 4, 459 (2008).

[23] J. Xing, L. D. Sanjeewa, J. Kim, G. R. Stewart, M.-H. Du, F. A. Reboredo, R. Custelcean, A. S. Sefat, Crystal Synthesis and Frustrated Magnetism in Triangular Lattice $CsRESe_2$ (RE = La–Lu): Quantum Spin Liquid Candidates $CsCeSe_2$ and $CsYbSe_2$, ACS Mat. Lett. DOI: 10.1021/acsmaterialslett.9b00464.

[24] M. Mekata, K. Adachi, Magnetic Structure of $CsCoCl_3$, J. Phys. Soc. Jpn. 44, 806 (1978).

[25] P. Lecheminant, B. Bernu, C. Lhuillier, L. Pierre, and P. Sindzingre, Order Versus Disorder in the Quantum Heisenberg Antiferromagnet on the Kagome Lattice using Exact Spectra Analysis, Phys. Rev. B 56, 2521 (1997).

[26] P. W. Anderson, The Resonating Valence Bond State in La_2CuO_4 and Superconductivity, Science 235, 1196 (1987).

[27] C. Kittel, Introduction to Solid State Physics, Eight Edition, John Wiley & Sons, Inc.

[28] W. D. Callister, Material Science and Engineering An Introduction, John Wiley & Sons. Inc, 7^{th} Edtion, 2007.

[29] K. Tomiyasu, J. Fukunaga, and H. Suzuki. Magnetic Short-range Order and Reentrant Spin-glass-like Behavior in $CoCr_2O_4$ and $MnCr_2O_4$ by Means of Neutron Scattering and Magnetization Measurements, Phys. Rev. B 70, 214434 (2004).

[30] L. Ballents, Spin Liquid in Frustrated Magnets, Nat. 464, 2010, DOI: 10.1038/nature08917.

[31] F. L. Pratt, P. J. Baker, S. J. Blundell, T. Lancaster, S. O. Kawamura, C. Baines, Y. Shimizu, K. Kanoda, I. Watanabe, G. Saito, Magnetic and Non-magnetic Phases of Quantum Spin Liquid, Nat. 471, 612 (2011).

[32] D. H. Zhou, E. S. Choi, G. Li, L. Balicas, C. R. Weibe, Y. Qui, J. R. D. Copley, J. S. Gardner, Spin Liquid State in the S=1/2 Triangular Lattice $Ba_2CuSb_2O_9$, Phys. Rev. Lett.

106, 147204 (2011).

[33] M. Blume, and Y. Hsieh, Biquadratic Exchange and Quadrupolar Ordering, J. of Appl. Phys. 40, 1249 (1969).

[34] H. H. Chen, and P. M. Levy, Quadrupole Phase Transition in Magnetic Solids, Phys. Rev. Lett. 27, 1383 (1971).

[35] A. Andreev and I. Grishchuk, Spin Nematics, J. of Expt. and Theo. Phys. 87, 467 (1984).

[36] T. Momoi, P. Sindzingre, and N. Shannon, Octupolar Order in the Multiple Spin Exchange Model on a Triangular Lattice, Phys. Rev. Lett. 97, 257204 (2006).

[37] E. M. Stoudenmire, S. Trebst, and L. Balents, Quadrupolar Correlations and Spin Freezing in $S = 1$ Triangular Lattice Antiferromagnets, Phys. Rev. B 79, 214436 (2009).

[38] N. Shannon, T. Momoi, and P. Sindzingre, Nematic Order in Square Lattice Frustrated Ferromagnets, Phys. Rev. Lett. 96, 027213 (2006).

[39] A. Mishra, M. Ma, F. C. Zhang, S. Guertler, L. H. Tang, and S. Wan, Directional Ordering of Fluctuation in Two Dimensional Compass Mod. Phys. Rev. Lett. 93, 207201 (2004).

[40] H. Tsunetsugu, and M. Arikawa, Spin Nematic Phase in $S = 1$ Triangular Antiferromagnets, J. of the Phys. Soc. of Jpn. 75, 083701 (2006).

[41] D. P. Landau, Theory of Magnetic Phase Transitions, Handbook of Magnetism and Advanced Magnetic Materials, Volume 1, John Wiley & Sons.

[42] S. Blundell, Magnetism in Condensed Matter (Oxford University Press), 2011.

[43] E. Connolly, Structure and Magnetic Properties of Model $S = 1/2$ and $S = 1$ Kagome Magnet, PhD Thesis, University College London, (2019).

[44] J. M. Kosterlitz, The Critical Properties of the Two-dimensional XY Model, J. Phys. C: Solid State Phys. 7, (1974).

[45] B. M. Bartlett, D. G. Nocera, Long-Range Magnetic Ordering in Iron Jarosites Prepared by Redox-Based Hydrothermal Methods, J. Am. Chem. Soc. 127, 8985 (2005).

[46] D. Grohol, D. G. Nocera, D. Papoutsakis, Magnetism of Pure Iron Jarosites, Phys. Rev. B

67, 064401 (2003).

[47] S.-H. Lee, C. Broholm, M. F. Collins, L. Heller, A. P. Ramirez, Ch. Kloc, E. Bucher, R. W. Erwin, and N. Lacevic, Less than 50% Sublattice Polarization in an Insulating *S* = 3/2 Kagomé Antiferromagnet at T≈0, Phys. Rev. B 56, 8091 (1997).

[48] D. Grohol, Q. Huang, B. H. Toby, J. W. Lynn, Y. S. Lee, and D. G. Nocera, Powder Neutron Diffraction Analysis and Magnetic Structure of Kagomé-type Vanadium Jarosite $NaV_3(OD)_6(SO4)_2$, Phys. Rev. B 68, 094404 (2003).

[49] T. Inami, M. Nishiyama, S. Maegawa, Magnetic Structure of the Kagomé Lattice Antiferromagnet Potassium Jarosite $KFe_3(OH)_6(SO_4)_2$, Phys. Rev. B 61, 12181 (2000).

[50] A. Chubukov, Order from Disorder in a Kagomé Antiferromagnet, Phys. Rev. Lett. 69, 832 (1992).

[51] Sachdev, Kagome´and Triangular-lattice Heisenberg Antiferromagnets: Ordering from Quantum Fluctuations and Quantum-disordered Ground States with Unconfined Bosonic Spinons, Phys. Rev. B 45, 12377 (1992).

[52] K. Matan, D. Grohol, D. G. Nocera, T. Yildirim, A. B. Harris, S. H. Lee, S. E. Nagler, and Y. S. Lee, Spin Waves in the Frustrated Kagomé Lattice Antiferromagnet $KFe_3(OH)_6(SO_4)_2$, Phys. Rev. Lett. 96, 247201 (2006).

[53] T. Yildirim, A. B. Harris, Magnetic Structure and Spin Waves in the Kagomé Jarosite Compound $KFe_3(SO_4)_2(OH)_6$, Phys. Rev. B 73, 214446 (2006).

[54] T. Inami, T. Morimoto, M. Nishiyama, S. Maegawa, Y. Oka, and H. Okumura, Magnetic Ordering in the Kagomé Lattice Antiferromagnet $KCr_3(OD)_6(SO_4)_2$, Phys. Rev. B 64, 054421 (2001).

[55] T. Morimoto, M. Nishiyama, S. Maegawa, and Y. Oka, Magnetization of New Kagomé Lattice Antiferromagnets: Cr-Jarosites, $ACr_3(OH)_6(SO_4)_2$ [A = Na, K, Rb, NH_4, J. Phys. Soc. Jpn. 72, 2085 (2003).

[56] A. S. Wills, Ph. D. Thesis, University of Edinburgh, Scotland, (1997).

[57] A. F. Wells, The Crystal Structure of Atacamite and the Crystal Chemistry of Cupric

Compounds, Acta. Cryst. 2, 175 (1949).

[58] F. C. Hawthorne, Refinement of the Crystal Structure of Botallackite, Min. Mag. 49, 87 (1985).

[59] M. E. Fleet, The Crystal Structure of Paratacamite, $Cu_2(OH)_3Cl$, Acta Crys. B 31, 183 (1975).

[60] X. G. Zheng, E. S. Otabe, Antiferromagnetic Transition in Atacamite $Cu_2Cl(OH)_3$, Solid State Comm. 130, 107 (2004).

[61] X. G. Zheng, C. N. Xu, Antiferromagnetic Transition in Botallackite $Cu_2Cl(OH)_3$, Solid State Comm. 131, 509 (2004).

[62] X. G. Zheng, T. Kawae, Y. Kashitani, C. S. Li, N. Tateiwa, K. Takeda, H. Yamada, C. N. Xu, and Y. Ren, Unconventional Magnetic Transitions in the Mineral Clinoatacamite $Cu_2Cl(OH)_3$, Phys. Rev. B 71, 052409 (2005).

[63] X. G. Zheng, M. Hagihala, K. Nishiyama, T. Kawae, Exotic Antiferromagnetic Transition in Deformed Pyrochlore Lattice $Ni_2(OH)_3Cl$ of Atacamite-structure, Phys. B 404, 677 (2009).

[64] D. Tsuneishi, M. Ioki, H. Kawamura, Novel Ordering of the Pyrochlore Heisenberg Antiferromagnet with the Ferromagnetic Next Nearest-neighbour Interaction, J. Phys. Cond. Matt. 19, 145273 (2007).

[65] X. G. Zheng, T. Kawae, H. Yamada, K. Nishiyama, and C. N. Xu, Coexisting Ferromagnetic Order and Disorder in a Uniform System of Hydroxyhalide $Co_2(OH)_3Cl$, Phys. Rev. Lett. 97, 247204 (2006).

[66] M. Fujihala, M. Hagihala, X. G. Zheng, and T. Kawae, Antiferromagnetic Magnetic Transition and Spin Fluctuations in the Deformed Pyrochlore Compound β-$Fe_2(OH)_3Cl$, Phys. Rev. B 82, 024425 (2010).

[67] M. Hagihala, X. G. Zheng, T. Toriyi, and T. Kawae, Antiferromagnetism and Geometric Frustration in Tetrahedral Lattice Hydroxyhalides $M_2(OH)_3Cl$, J. of Phys.: Cond. Matter. 19, 145281 (2007).

[68] M. J. Harris, S. T. Bramwell, D. F. McMorrow, T. Zeiske, K. W. Godfrey, Geometrical Frustration in the Ferromagnetic Pyrochlore $Ho_2Ti_2O_7$, Phys. Rev. Lett. 79, 2554 (1997).

[69] M. P. Shores, E. A. Nytko, B. M. Bartlett, and D. G. Nocera, A Structurally Perfect *S* = 1/2 Kagome Antiferromagnet, J. of Am. Chem. Soc., 127, 13462 (2005).

[70] M. A. de Vries, J. R. Stewart, P. P. Deen, J. O. Piatek, G. J. Nilsen, H. M. Harrison, Scale-Free Antiferromagnetic Fluctuations in the *S* = 1/2 Kagome Antiferromagnet Herbertsmithite, A. Phys. Rev. Lett. 103, 237201 (2009).

[71] S. H. Lee, H. Kikuchi, Y. Qui, B. Lake, Q. Huang, K. Habicht, K. Kiefer, Quantum-spin-liquid States in the Two-dimensional Kagome Antiferromagnets $Zn_xCu_{4-x}(OD)_6Cl_2$, Nat. Mat. 6, 853 (2007).

[72] A. Olariu, P. Mendels, F. Bert, F. Duc, J. Trombe, M. A. de Vries, and A. Harrison, ^{17}O NMR Study of the Intrinsic Magnetic Susceptibility and Spin Dynamics of the Quantum Kagome Antiferromagnet $ZnCu_3(OH)_6Cl_2$, Phys. Rev. Lett. 100, 087202 (2008).

[73] J. S. Helton, K. Maton, M. P. Shores, E. A. Nytko, B. M. Bartlett, Y. Yoshida, Y. Takano, A. Suslov, Y. Qui, J. H. Chung, D. A. Nocera, Y. S. Less, Spin Dynamics of the Spin-1/2 Kagome Lattice Antiferromagnet $ZnCu_3(OH)_6Cl_2$, Phys. Rev. Lett., 98, 107204 (2007).

[74] A. Zorko, S. Nelluta, J. van Toll, L. C. Brunel, F. Bert, F. Duc, J. C. Trombe, M. A. de Vries, A. Harrison, and P. Mendels, Dzyaloshinsky-Moriya Anisotropy in the Spin-1/2 Kagome Compound $ZnCu_3(OH)_6Cl_2$, Phys. Rev. Lett. 101, 026405 (2008).

[75] B. Fåk, E. Kermarrec, L. Messio, B. Bernu, C. Lhuillier, F. Bert, P. Mendels, B. Koteswararao, F. Bouquet, J. Ollivier, A. D. Hillier, A. Amato, R. H. Colman, and A. S. Wills, Kapellasite: A Kagome Quantum Spin Liquid with Competing Interactions, Phys. Rev. Let. 109, 037208 (2012).

[76] M. Fujihala, X. G. Zheng, Y. Oohara, H. Morodomi, T. Kawae, Akira Matsuo, and Koichi Kindo, Short-range Correlations and Persistent Spin Fluctuations in the

Undistorted Kagome Lattice Ising Antiferromagnet $Co_3Mg(OH)_6Cl_2$, Phys. Rev. B, 85, 012402 (2012).

[77] S. E. Dissanayake, C. Chan, S. Ji, J. Lee, Y. Qiu, K. C. Rule, B. Lake, M. Green, M. Hagihala, X. G. Zheng, T. K. Ng, and S. H. Lee, Magnetic-field-induced Instability of the Cooperative Paramagnetic State in $Zn_xCo_{4-x}(OD)_6Cl_2$, Phys. Rev. B 85, 174435 (2012).

[78] J. Merino, and A. Ralko, Role of Quantum Fluctuations on Spin Liquids and Ordered Phases in the Heisenberg Model on the Honeycomb Lattice, Phys. Rev. B 97, 205112 (2018).

[79] A. S. Will, A. Harrison, S. A. M. Mentink, T. E. Mason, and Z. Tun, Magnetic Correlations in Deuteronium Jarosite, a model $S = 5/2$ Kagomé Antiferromagnet, Europhys. Lett. 42, 325 (1998).

[80] D. Coffey, T. M. Rice, and F. C. Zhang, Phys. Dzyaloshinskii-Moriya Interaction in Cuprates, Phys. Rev. B 44, 10112 (1991).

[81] M. Elhajal, B. Canals, and C. Lacroix, Symmetry Breaking due to Dzyaloshinsky-Moriya Interactions in the Kagome´ Lattice, Phys. Rev. B 66, 014422 (2002).

[82] J. T. Chalker, P. C. W. Holdsworth, and E. F. Shender, Hidden Order in a Frustrated System: Properties of the Heisenberg Kagomé antiferromagnet, Phys. Rev. Lett. 68, 855 (1992).

[83] G.-W. Chern and R. Moessner, Dipolar Order by Disorder in the Classical Heisenberg Antiferromagnet on the Kagome Lattice, Phys. Rev. Lett. 110, 077201 (2013).

[84] M. Maksymenko, V. R. Chandra, and R. Moessner, Classical Dipoles on the Kagome Lattice, Phys. Rev. B 91, 184407 (2015).

[85] R. Moessner, and J. T. Chalker, Low-temperature Properties of Classical Geometrically Frustrated Antiferromagnets, Phys. Rev. B 58, 12049 (1998).

[86] A. B. Harris, C. Kallin, and A. J. Berlinsky, Possible Néel Orderings of the Kagomé Antiferromagnet, Phys. Rev. B 45, 2899 (1992).

[87] J.-C. Domenge, P. Sindzingre, C. Lhuillier, and L. Pierre, Twelve sublattice Ordered Phase in the J_1-J_2 Model on the Kagomé Lattice, Phys. Rev. B 72, 024433 (2005).

[88] K. Kano, and S. Nava, Prog. Analytical Representration of General Spin, In Theor. Phys. 10, 158 (1953).

[89] D. A. Huse and A. D. Rutenberg, Classical Antiferromagnets on Kagome Lattice, Phys. Rev. B 45, 7536 (1992).

[90] I. A. Chioar, N. Rougemaille, and B. Canals, Ground-state Candidate for the Classical Dipolar Kagome Ising Antiferromagnet, Phys. Rev. B 93, 214410 (2016).

[91] R. Moessner, S. L. Sondhi, and P. Chandra, Two-Dimensional Periodic Frustrated Ising Models in a Transverse Field, Phys. Rev. Lett. 84, 4457 (2000).

[92] R. Moessner, and S. L. Sondhi, Ising Models of Quantum Frustration, Phys. Rev. B 63, 224401 (2001).

[93] G. Shirane, S. M. Shapiro, J. M. Tranquada, Neutron Scattering with a Triple-Axis Spectrometer Basic Technique, Cambridge University Press, (2002).

[94] I. M. Sosnowska, The birth of time-of-flight (TOF) Neutron Powder Diffraction at Pulsed Neutron Source (invited), Cryst. Res. Technol. 50, 705 (2015).

[95] E. O. Wollan, and C. G. Shull, The Diffraction of Neutrons by Crystalline Powders, Phys. Rev. 73, 830 (1948). D. J. Hughes, Neutron optics, (New York, London, Interscience Publishers, (1954).

[96] T. Kamiyama, Quick Guide, Z-Rietveld for Windows, Version. 1.0, www.z-code.kek.jp/zrg.

[97] ISIS HRPD User Manual http://www.isis.stfc.ac.uk/instruments/hrpd/documents/hrpd-manual6735.pdf.

[98] H. M. Rietveld, A Profile Refinement Method for Nclear and Magnetic Structures", J. of Appl. Cryst. 2, 65 (1969).

[99] F. Izumi, and K. Momma, Three-Dimensional Visualization in Powder Diffraction Solid State Phenom, 130, 15 (2007).

[100] A. C. Larson, R. B. Von Dreele, Los Alamos National Laboratory Report LAUR, 2004, 86.

[101] J. Rodriguez-Carvajal, Recent Advances in Magnetic Structure Determination by Neutron Powder Diffraction, J. Phys. B: Cond. Mat., 192, 55 (1993).

[102] R. Oishi, M. Yonemura, Y. Nishimaki, S. Toriia, .Hoshikawa, T. Ishigaki, T. Morishima, K. Mori, T. Kamiyama, Nuclear Instruments and Methods in Physics Research Section A, 600 (1), pp. 94-96 (2009).

[103] Y. A. Izymov, V. E. Naish and R. P. Ozerov, 'Neutron Diffraction of Magnetic Materials', Consultants Bureau, New York, 1991.

[104] E. F. Bertaut, Lattice Theory of Spin Configuration, J. of Appl. Phys. 33, 1138 (1962).

[105] E. F. Bertaut, Representation Analysis of Magnetic Structures, Acta Cryst. A, 24, 217 (1968).

[106] E. F. Bertaut, Magnetic Structure and Group Theory, J. de Phys. Colloque C1, 462 (1971).

[107] E. F. Bertaut, On Group Theoretical Techniques in Magnetic Structure Analysis, J. of Mag. and Mag. Mat. 24, 267 (1981).

[108] Y. A. Izyumov, and V. E. Naish, Phase Transition and Crystal Structure, J. Mag. and Mag. Mat. 12, 239 (1979).

[109] E. Hovestreydt, M. Aroyo, S. Sattler, H. Wondratschek, KAREP - a Program for Calculating Irreducible Space-group Representations, J. of Appl. Cryst. 25, 544 (1992).

[110] J. Rodriguez-Carvajal, unpublished work.

[111] P. Czapnik, and W. Sikora, unpublished work.

[112] A. S. Wills, A New Protocol for the Determination of Magnetic Structures Using Simulated Annealing and Representational Analysis (SARA*h*), Physica B 680, 276 (2000).

[113] R. L. Fagaly, Supercoonducting Quantum Interface Device Instruments and Applications, Rev. of Sci. Inst. 77, 101101 (2006).

[114] K. Zenmyo, H. Kubo, M. Tokita, T. Hamasaki, M. Hagihala, and X. G. Zheng, Proton NMR Study of Pyrochlore-Like Atacamite $Mn_2Cl(OH)_3$J. Phys. Soc. Jpn. 80, 024704 (2011).

[115] X. Feng, Y. Deng, and H. W. J. Blöte, Percolation Transitions in Two Dimensions, Phys. Rev. E 78, 031136 (2008).

[116] X.- G. Zheng, I. Yamauchi, S. Kitajima, M. Fujihala, M. Maki, S. Lee, M. Hagihala, S. Torii, T. Kamiyama, and T. Kawae, Two-dimensional Triangular-lattice Cu(OH)Cl, Belloite, as a Magnetodielectric System, Phys. Rev. Mater. 2, 104401 (2018).

[117] L. F. Feiner, A. M. Oles, and J. Zaanen, Quantum Melting of Magnetic Order due to Orbital Fluctuations, Phys. Rev. Lett. 78, 2799 (1997).

[118] F. Reynaud, D. Mertz, F. Celestini, J.-M. Debierre, A. M. Ghorayeb, P. Simon, A. Stepanov, J. Voiron, and C. Delmas, Quantum Melting of Magnetic Order due to Orbital Fluctuations, Phys. Rev. Lett. 86, 3638 (2001).

[119] S. de Brion, M. D. Nunez-Regueiro, and G. Chouteau, Frontiers in Magnetic Materials (edited by A. V. Narlikar, Springer, Berlin, 2005).

[120] X. Sun, E. Feng, Y. Su, K. Nemkovski, O. Petracic, and T. Brückel, Magnetic Properties and Spin Structure of MnO Single Crystal and Powder, J. Phys.: Conf. Ser., 862, 012027 (2017).

[121] H. Guo, K. Manna, H. Luetkens, H. Hoelzel, and A.C. Komarek, Phys. Spin Glass Behavior in $LaCo_{1-x}Rh_xO3$ (x=0.4, 0.5, and 0.6), Phys. Rev. B 94, 205128, (2016).

[122] A. Marcinkova, T. C. Hansen, C. Curfs, S. Margadonna, and J. W. G. Bos, Nd induced Mn Spin Reorientation Transition in NdMnAsO, Phys. Rev. B, 82, 174438 (2010).

[123] M. Hagihala, X. G. Zheng, T. Kawae, and T. J. Sato, Successive Antiferromagnetic Transitions with Multi-k and Noncoplanar Spin Order, Spin Fluctuations, and Field-Induced Phases in Deformed Pyrochlore Compound $Co_2(OH)_3Br$, Phys. Rev. B 82, 214424 (2010).

[124] H. Kawamura, Monte Carlo Study of Chiral Criticality –XY and Heisenberg Stacked-

Triangular Antiferromagnet, J. Phys. Soc. Jpn. 61, 1299 (1992).

[125] H. Kawamura and S. Miyashita, Phase Transition of the Two-Dimensional Heisenberg Antiferromagnet on the Triangular Lattice, J. Phys. Soc. Jpn. 53, 4138 (1984).

[126] J. C. LeGuillou and J. Zinn-Justin, Phys. Critical Exponent from Field Theory, Phys. Rev. B 21, 3976 (1980).

[127] J. C. Le Guillou and J. Zinn-Justin, Accurate Critical Exponents from Field Theory, J. Phys. 50, 1365 (1989).

[128] M. Nishiyama, S. Maegawa, T. Inami, and Y. Oka, Phys. Magnetic Ordering and Spin Dynamics in Potassium Jarosite: A Heisenberg Kagomé Lattice Antiferromagnet, Phys. Rev. B 67, 224435 (2003).

[129] H. Ishikawa, T. Okubo, Y. Okamoto, and Z. Hiroi, Kagome–Triangular Lattice Antiferromagnet $NaBa_2Mn_3F_{11,}$ J. Phys. Soc. Jpn 83, 043703 (2014).

[130] M. Hagihala, S. Hayashida, M. Avdeev, H. Manaka, H. Kikuchi, and T. Masuda, Magnetic States of Coupled Spin Tubes with Frustrated Geometry in $CsCrF_{4,}$ npj Quantum Mater. 4, 14 (2019).

The author's related publications

List of Published Research Article

1. **Md. Mahbubur Rahman Bhuiyan**, Xu-Guang Zheng, Masato Hagihala, Suki Torii, Takashi Kamiyama, and Tatsuya Kawae, Spin order in the classical spin kagome antiferromagnet $Mg_xMn_{4-x}(OH)_6Cl_2$, Physical Review B 101, 134424 (2020).

International Conference Attained

1. **Md. Mahbubur Rahman Bhuiyan**, Ichihiro Yamauchi, Xu-Guang Zheng, and T. Kawae, Magnetism in Kagome Antiferromagnet $MgMn_3(OH)_6Cl_2$, The 3rd J-PARC Symposium, September 23-26, 2019, Tsukuba, Japan.

2. **Md. Mahbubur Rahman Bhuiyan**, I. Yamauchi, X. G. Zheng, M. Hagihala, S. Torii, and T. Kamiyama, Synthesis and magnetism of $MgMn_3(OH)_6Cl_2$, a quasi-classical spin kagome Antiferromagnet, Taiwan-Japan International Workshop, Kyushu Branch Japanese Physical Society, 30th November, 2019, Saga University (Saga, JAPAN).

Acknowledgement

I am very much pleased to be one of the Doctoral students at the Department of Physics at Saga University and would like to acknowledge the contribution of all persons involved with my research work during my study period.

Firstly, I would like to express my heartfelt respect, the deep sense of gratitude, and immense indebtedness to my academic supervisor Professor Xu-Guang Zheng, a Condensed matter scientist at the Department of Physics, Saga University for his precious suggestions, sincere guidance and continuous encouragement during the entire period of the research work. I am very much appreciated to his advice in research as well as careful consideration of my future research continuity in my home county. Moreover, I would also like to thank him for the continuous support and interest in a safe and comfortable life for me in- and outside the campus.

I would like to thank my doctoral study's co-supervisor, Makoto Maki, Associate Professor, Department of Physics, Saga University, Japan; and Ichihiro Yamauchi, Associate Professor, Saga University, Japan for their support during my study period. I am incredibly thankful to Ichihiro Yamauchi for teaching me how to analyze data by Igor Pro software and provide some valuable knowledge.

I am thankful to Tatsuya Kawae, Associate Professor, Department of Applied Quantum Physics, Kyushu University, to carry out a temperature-dependent magnetic measurement using the Magnetic Property Measurement System (MPMS) based on SQUID.

I acknowledge the support of Professor Takashi Kamiyama, Professor, Institute of Materials Structure Science, KEK, Tokai; Masato Hagihara, Assistant Professor, Institute of Materials Structure Science, KEK, Tokai, and Shuki Torii, Researcher, Institute of Materials Structure Science, KEK, Tokai to allow me to carry out neutron powder experiment as well as giving valuable suggestion during the neutron diffraction experiment.

I am grateful to Ms. Misako Tsuji, Administrative officer, Department of Physics, Saga University for her kind administrative support during my study period.

I am thankful to Takahiro Yuasa, a graduate student (at present Engineer, KEK, Japan) who served as a tutor for me and assisted me in my few laboratories works during my study period. Actually, the help of Mr. Yuasa san made my Japanese life very easy. I am also grateful to Takero Numano, Master Student, for his help during my stay in Japan.

I acknowledge the financial support of Bangabandhu Science and Technology Fellowship Trust, Ministry of Science and Technology, Government of the People's Republic of Bangladesh for giving me a scholarship to carry-out my doctoral study at Saga University, Japan.

I have my most profound appreciation and heartfelt thanks for my parents, elder brother, elder sister, wife, son (Manaf kun), and all other family members for their love, inspirations, and sacrifice throughout my study.

Finally, I am very grateful to all Japanese citizens who behaved gently with me during my study period in Japan.

Md. Mahbubur Rahman Bhuiyan

SEPTEMBER-2020